SEPTEMBER 1970

MDC G1403

FACILITY FORM 602
N70-38148 (ACCESSION NUMBER)
37 (PAGES)
CR-112967 (NASA CR OR TMX OR AD NUMBER)
(THRU) 1
(CODE) 30
(CATEGORY)

EXPERIMENTAL INVESTIGATION OF ULTRAHIGH VACUUM ADHESION AS RELATED TO THE LUNAR SURFACE

FINAL CONTRACT REPORT
Fifth Year Summary
1 January 1969 Through 19 June 1970

MCDONNELL DOUGLAS ASTRONAUTICS COMPANY

MCDONNELL DOUGLAS CORPORATION

https://ntrs.nasa.gov/search.jsp?R=19700028832 2020-03-11T22:55:02+00:00Z

MCDONNELL DOUGLAS

EXPERIMENTAL INVESTIGATION OF ULTRAHIGH VACUUM ADHESION AS RELATED TO THE LUNAR SURFACE

FINAL CONTRACT REPORT
FIFTH YEAR SUMMARY
1 JANUARY 1969 THROUGH 19 JUNE 1970

SEPTEMBER 1970

MDC G1403

PREPARED BY:

J. J. GROSSMAN
PRINCIPAL INVESTIGATOR

J. A. RYAN
M. W. WEGNER
CO-PRINCIPAL INVESTIGATORS

SPACE SCIENCES DEPARTMENT
RESEARCH AND DEVELOPMENT SUBDIVISION

PREPARED FOR:

NATIONAL AERONAUTICS AND SPACE ADMINISTRATION
OFFICE OF RESEARCH AND TECHNOLOGY
WASHINGTON, D.C.
CONTRACT NUMBER:
NAS7-307 (DATE OF ISSUE 26 JUNE 1964)

MCDONNELL DOUGLAS ASTRONAUTICS COMPANY-WEST

5301 Bolsa Avenue, Huntington Beach, CA 92647

PRECEDING PAGE BLANK NOT FILMED.

PREFACE

This report presents and summarizes work performed by the Space Sciences Department, McDonnell Douglas Astronautics Company--West, for the National Aeronautics and Space Administration's Office of Advanced Research and Technology under Contract NAS7-307. The work consisted of experimental investigations of etching techniques to reveal the defect structure of minerals, electrical charge distributions of ultrahigh vacuum cleaved crystals and fractured rocks, and ultrahigh vacuum adhesion as related to the lunar surface.

CONTENTS

	LIST OF FIGURES	v
Section 1	INTRODUCTION	1
	1.1 General	1
	1.2 Objectives	1
	1.3 Approach	1
	1.4 Items of Interest	2
Section 2	INSTRUMENT AND TECHNIQUES	3
	2.1 Defect Etching	3
	2.2 Electrostatic Charging	5
	2.3 Silicate Adhesion	9
Section 3	EXPERIMENTAL RESULTS	10
	3.1 Defect Etching	10
	3.2 Electrostatic Charging	25
	3.3 Silicate Adhesion	36
Section 4	DISCUSSION	38
	4.1 Defect Etching	38
	4.2 Electrostatic Charging	39
	4.3 Silicate Adhesion	41
Section 5	SUMMARY	44
Appendix A	LUNAR SOIL ADHESION DUE TO ELECTROSTATIC FORCES STABILIZIED BY SOLAR RADIATION	46
		46
	REFERENCES	51

FIGURES

1	Successive Etching of Olivine Crystal (010)	4
2	Transmission Electron Micrograph of Albite Perthite in Orthoclase	6
3	Transmission Electron Micrographs of Defects in Albite (a) Antiphase Boundaries; (b) Screw Dislocation Crossing a Twin Boundary; (c) Complex Dislocation Network	7
4	Matched (111) Faces; CaF_2 Cleavage Etched Simultaneously, Symmetrical Triangular Etch Pitch Shape Suggests They are <011> (110) Edge Dislocations	8
5	Dislocations at Microperthite Boundaries of Orthoclase (001) and (010)	11
6	Microcracks Crossing Perthite Boundary into Orthoclase Matrix (001)	12
7	Albite (001), (a) Polygonized Dislocations, (b) A Twin Band Displaced Laterally by an Irregular Deformation Slip Plane	14
8	Albite (001) Deformation Bands. Same Crystal as Figure 7 at Lower Magnification	15
9	Albite (001), Etched Antiphase Boundaries	16
10	Diopside (100). (a) Quadrilateral Etch Figures with Mirror Symmetry, (b) Polygonized Etch Figures	17
11	Hypersthene (a) (111) Face Etched with HF, HNO_3, HOAc, (1:1:4), (b) (100) Face Etched with Concentrated HF	19
12	Low Angle <100> Tilt Boundaries on (010) Olivine	20
13	Very Low Angle <100> Tilt Boundaries on (010) Olivine	21
14	Polygonized Dislocations Adjacent to a Low Angle <100> Boundary on (010) Olivine	22
15	Olivine (001), Etched	23

16	Fission Tracks in Etched Biotite Mica Magnification	24
17	Etch Figures on (111) CaF_2 Cleavage, Run No. E-13. (a) Deformation from Knife and Anvil Cleavage. (b) Dislocation Pileup at Fault Located in Same Area as the Positive Peak Shown in Figure 18	26
18	Photomicrographs of Defects Due to Knife During (111) CaF_2 Cleavage, Run No. E-13	27
19	Electrostatic Charge Isodensity Distribution on (111) Cleaved CaF_2 Crystal, Run No. E-13	28
20	Variation in Peak to Valley Charge Difference with Time for CaF_2 and Granite Cleavages	31
21	Variation in Charge Distributions with Angle for LiF Cleavage No. E-14 at a Series of Times After Cleavage	33
22	Variation with Time for LiF Peaks Run No. E-14. Peak Numbers are Identified in Figure 21	34
23	Charge Isodensity Distribution Curves for Granite Fracture Run No. E-15. Photomicrograph Insert Shows Topological Features	35
A-1	Photoelectric Currents Produced on the Lunar Surface by Solar UV Radiation from Adjacent Particles with Different Work Functions W_1 and W_2	47

Section 1
INTRODUCTION

1.1 GENERAL

This report presents a summary of work accomplished during the period 1 January 1969 through 19 June 1970, on the study of the ultrahigh vacuum adhesion of silicates as related to the lunar surface. This work has been conducted for the Office of Advanced Research and Technology, National Aeronautics and Space Administration, under Contract NAS7-307.

1.2 OBJECTIVES

The general purposes of this program were: (1) to obtain quantitative experimental data concerning the origin of the electrical charge distribution produced by the ultrahigh vacuum fracture of various silicate minerals and model materials, (2) to achieve an understanding of the mechanisms responsible for the observed charge stability in relationship to the lunar environment, (3) to apply etching techniques to a variety of possible lunar silicates including shock-loaded and/or radiation damaged materials, also vacuum cleaved silicates and model crystals, (4) to apply the results to further understanding of the possible effects of environment on silicate structure, in preparation for analyzing the lunar materials returned by Apollo, and (5) to attempt to obtain information concerning bonding of crystal grains in polycrystalline rocks.

1.3 APPROACH

The approach used during this report period has been (1) to cleave silicates at ultrahigh vacuum and measure the electrostatic charge distribution produced, (2) to obtain microchemical and microphysical profiles on the cleaved surfaces, (3) to apply defect etching techniques to a variety of possible lunar silicates, and (4) to measure the adhesion force of polycrystalline silicates fractured at ultrahigh vacuum.

Approach (1) serves to provide information on the origin and dynamics of the observed electrostatic charging in dielectrics cleaved in ultrahigh vacuum. Approaches (2) and (3) serve to provide direct evidence of the relative roles played by composition gradients, dislocations, and stress patterns in electrostatic charging. Approach (4) serves to provide information on behavioral differences between single and polycrystalline silicates.

1.4 ITEMS OF INTEREST

To date, the following publications and presentations have resulted from material contained in this report.

Ryan, J. A. and J. J. Grossman, Adhesion of Silicates, invited paper presented at Physics of Adhesion Symposium, Karlsruhe, Germany, 1969 (in press).

Grossman, J. J., Ultrahigh Vacuum Adhesion, invited lecture at Carnegie-Mellon University, Pittsburgh, Pennsylvania, 1969.

Grossman, J. J., Electrostatic Charge Distribution on Ultrahigh Vacuum Cleaved Silicates, J. Vac. Sic, and Tech., 6, 203-206, 1969.

Wegner, M. W. and J. J. Grossman, Dislocation Etching of Naturally Deformed Olivine, Trans. Amer. Geophys. Union, 50, 676, 1969.

Ryan, J. A. and J. J. Grossman, Comments on Lunar Surface Adhesion, presented at Working Group on Extraterrestrial Resources Symposium, Denver, Colorado, 1969 (in press).

Ryan, J. A., Adhesion Characteristics of Lunar Rock, presented at American Vacuum Society Meeting, Anaheim, California, 1970.

Grossman, J. J., Hansen, W. M., and Wegner, M. W. (1969) Electrostatic Charge Distribution Measurements on UHV Cleaved Dielectrics, American Vacuum Society Symposium, May 7, Los Angeles, California.

Section 2
INSTRUMENTATION AND TECHNIQUES

2.1 DEFECT ETCHING

Chemical etching techniques were utilized to survey crystalline defects in rock-forming silicate minerals and model crystals, and to study defects resulting from ultrahigh vacuum cleavage of these materials. A description of the silicates, their structures and sources was presented in the First Year Summary of this program.

The etch studies were conducted on air-cleaved crystal surfaces, utilizing preferred cleavage orientations, on crystals encapsulated in plastic and polished on different low-index faces, and on crystal surfaces cleaved in ultrahigh vacuum. Factors in choosing etch compositions selective to dislocations in the crystals were: the slight solubility of silicates in dilute hydrofluoric and fluosilicic acids, and in hot sodium hydroxide solutions; complexing of the crystal cations with various organic acids; and the addition of inhibiting salts whose cation radii are close to those of the crystal cations. A Leitz Dialux-Pol microscope and a Hitachi HU-11A electron microscope were used for petrography and for detailed surface studies of defect structures of the crystals after etching. Chemical composition profiles were examined with an ARL electron microprobe X-ray analyzer. An optical goniometer and a General Electric Model XRD-6 X-ray diffractometer were used to establish crystallographic orientation of the crystals.

Non-destructive methods for replication of surfaces for examination by electron microscopy were perfected. The basic technique consisted of depositing first a carbon-platinum coating, then forming a composite of thin plastic layers on the coating to permit its removal, and finally, dissolving the plastic. This method of replication allowed dislocation lines to be traced through the crystal by successive polishing and selective chemical etching (Figure 1). A means for obtaining transmission electron micrographs of minerals

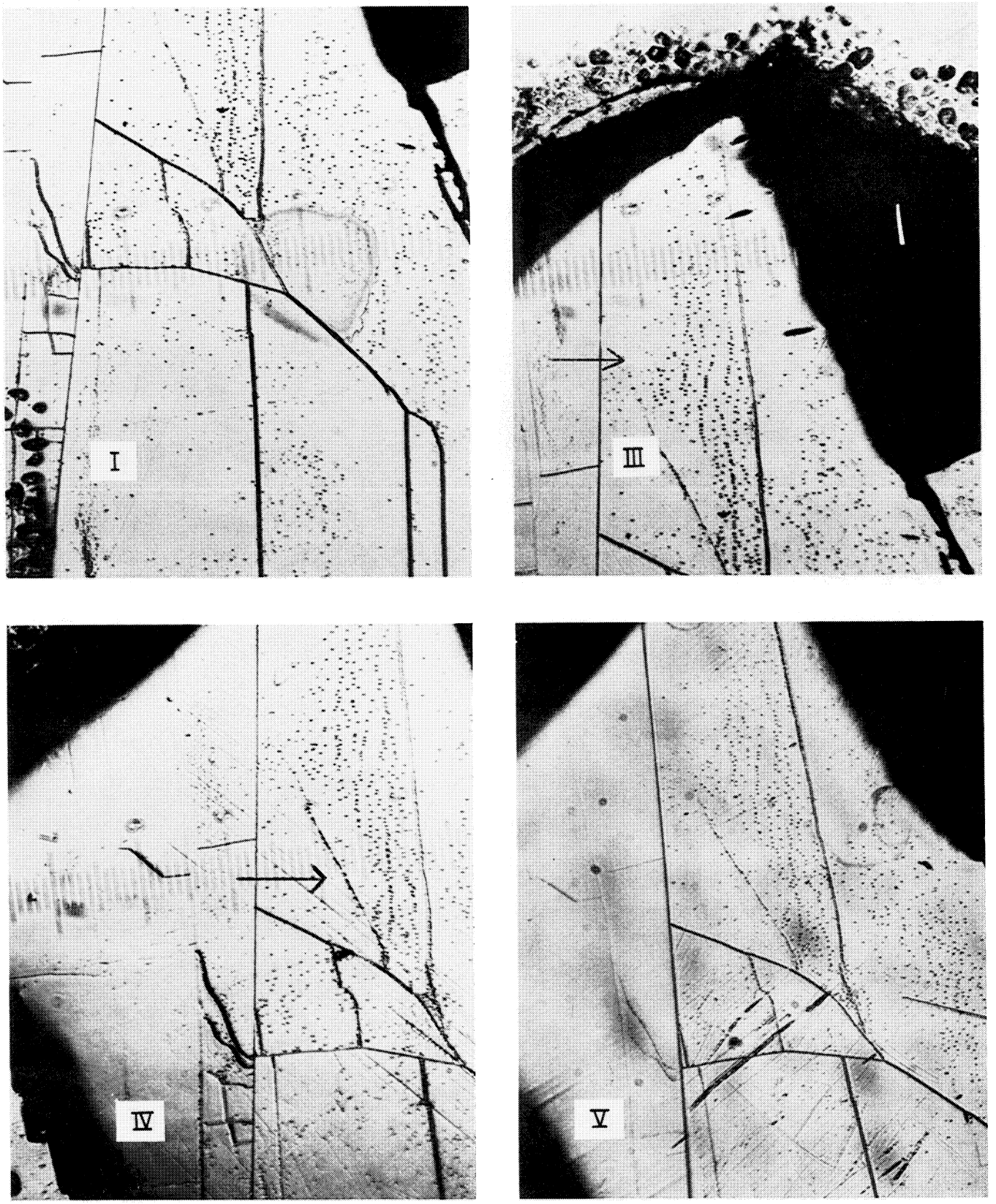

Figure 1. Successive Etching of Olivine Crystal (010)

such as orthoclase and albite, which have an easy cleavage plane, was devised. It consisted of bonding a thick plastic coating directly to the cleavage face and then stripping off and disolving the plastic. This stripping removes a thin crystal layer. Micrographs obtained after utilization of this technique are shown in Figures 2 and 3.

Chemical etching of matching faces of cleaved crystals was performed, confirming the selectivity of the etchants to dislocations (Figure 4).

A method for encapsulating, polishing and etching small grains was perfected. Peridot crystalline aggregates, and a peridotite nodule, composed of olivine, enstatite and chrome diopside were covered with a low viscosity, low temperature, epoxy resin. A low vacuum was applied and the resin cured slowly at 50°C. This work was a preliminary study in preparation for the lunar rock analysis and study of interfaces between small crystalline particles.

2.2 ELECTROSTATIC CHARGING

A detailed analysis of the cartesian cross configuration for measuring isoelectric charge distributions revealed two unexpected experimental sources of error which degraded the charge-density profile position accuracy. Both are connected with the magnetically coupled ultrahigh vacuum rotary feedthrough.

The rotary shaft ball bearing races were not concentric so that the center of rotation of the crystal swept out a conical arc approximately one probe diameter (0.75 mm). In addition, free play between the ball bearings and the race caused the magnet coupling to shift the crystal mounting shaft in arbitrary direction of 0.08 mm.

Data reduction of isoelectric charge distribution curves must take into consideration the trajectory of the electrometer probe as it is translated linearly toward the center of rotation of the crystal. If it is displaced some minimum distance d above and below the center, then the actual angular shift θ between the probe location and the recorder-indicated chart position is given by $\tan \theta = d/R$ where R is the apparent radial location. This correction has been applied to all the experimental data using various but equivalent techniques.

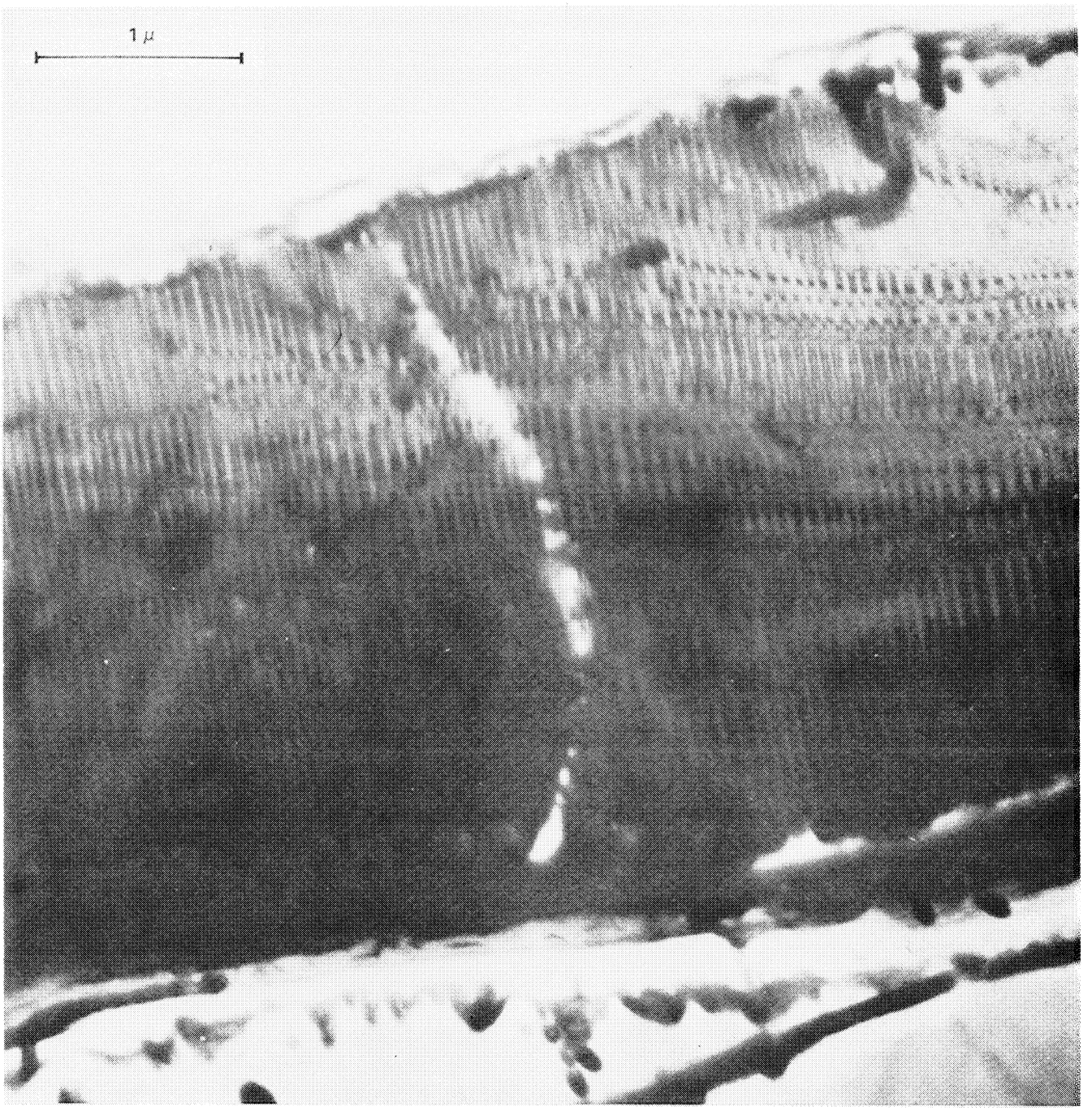

Figure 2. Transmission Electron Micrograph of Albite Perthite in Orthoclase

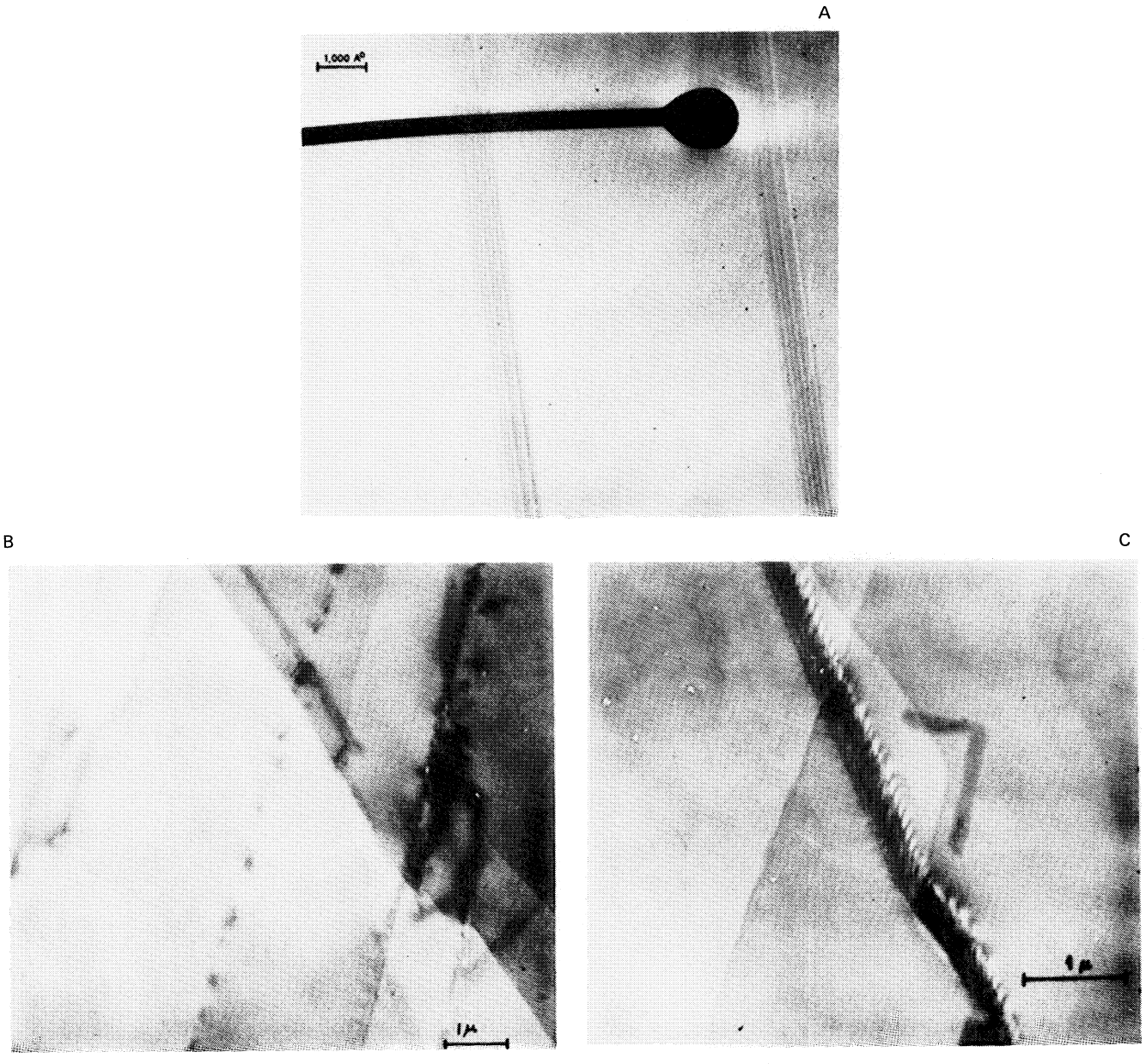

Figure 3. Transmission Electron Micrographs of Defects in Albite. (a) Antiphase Boundaries; (b) Screw Dislocation Crossing a Twin Boundary; (c) Complex Dislocation Network

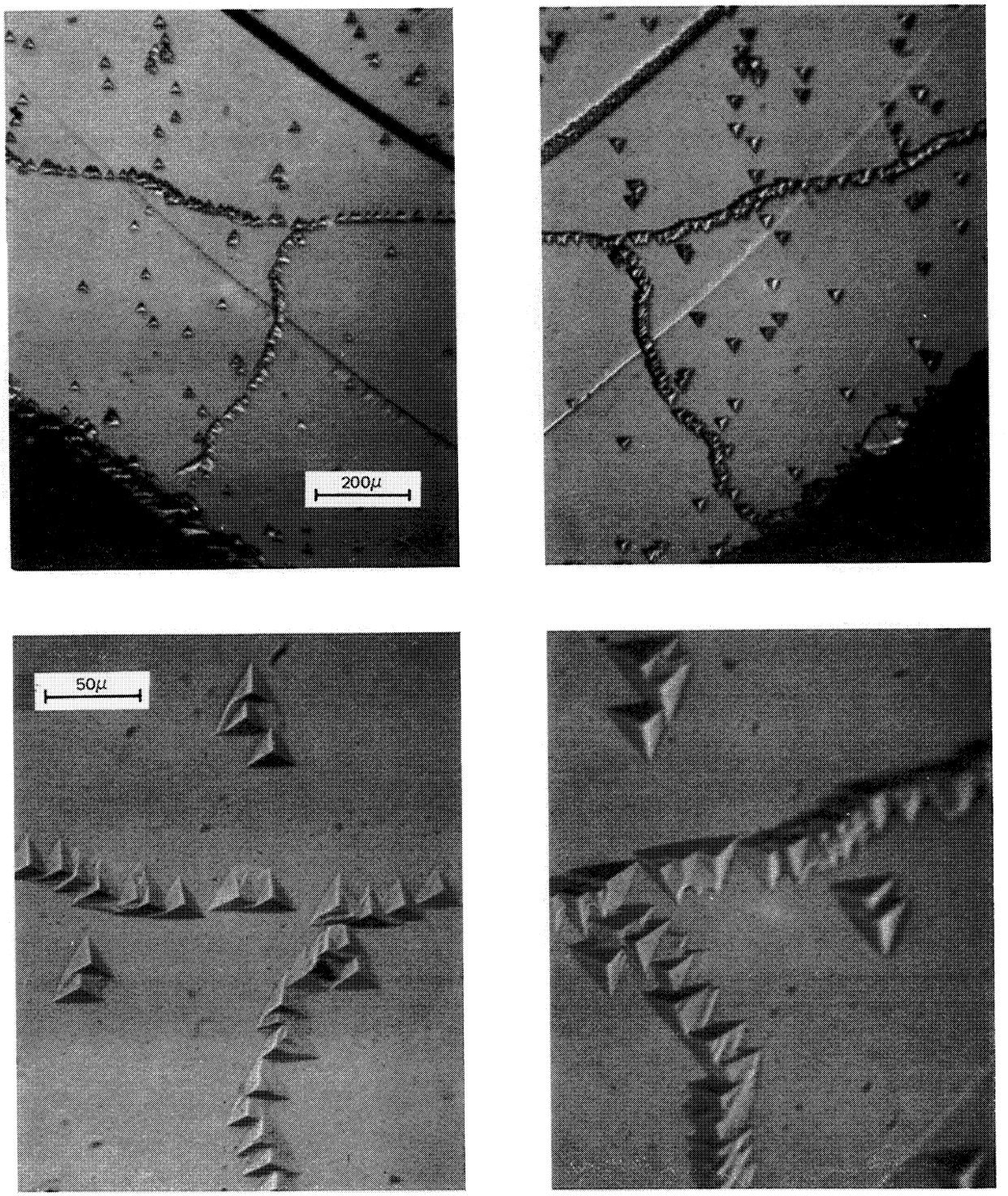

Figure 4. Matched (111) Faces; CaF_2 Cleavage Etched Simultaneously, Symmetrical Triangular Etch Pitch Shape Suggests They are <011> (110) Edge Dislocations

The notch cleavage system used for brittle fracture of mineral silicates was not successful with CaF_2. The tendency to fracture along intersecting (111) faces produced uncontrolled steps, e.g., in E-11 steps 500 μm high. The E-11 high point exhibited a strong positive peak positioned approximately 120 degrees from the cleavage slot (see Figure 2, Eighteenth Quarterly Report). A secondary maximum was found 120 degrees from both of these points.

A modified anvil and chisel system was developed and tested in air. The anvil had a rounded saddle shape to prevent sharp edges touching the crystal. Sharp edges are characteristic of the V-slotted anvil used with the silicate minerals. A single edge razor blade was substituted for the chisel. Without using a notch, it was possible to get a perfect cleavage, if the direction was $<\bar{1}\bar{1}2>$, in air. This system was finally adopted for UHV CaF_2 and LiF cleavages.

2.3 SILICATE ADHESION

Direct measurement of silicate adhesion constituted only a very small portion of the year's work. Two minor modifications were made in the experimental apparatus. The first consited of changing the sample mounting procedure from mechanical clamping to epoxy bonding (Torr Seal; vapor pressure $<10^{-9}$ torr). This was done in preparation for the Apollo lunar samples which were expected to be highly irregular in shape. The second consisted of attaching the electrometer probe assembly to the adhesion measuring system. This was also done in preparation for the Apollo samples, to free the second vacuum system.

Section 3
EXPERIMENTAL RESULTS

3.1 DEFECT ETCHING

The chemical etching survey of crystalline structure defects in silicate minerals included the feldspars (orthoclase and albite), the micas, the pyroxenes, and the orthosilicates. The model crystal, used in ultrahigh vacuum cleavage studies was calcium fluoride, a high purity single crystal obtained from Harshaw. Preferential etchants consisted of combinations of hydrofluoric, hydrochloric, nitric and citric acids used at room temperature, and hot sodium and potassium hydroxides.

Orthoclase ($K\,Al\,Si_3\,O_8$), cleaved in ultrahigh vacuum for the electrostatic charging study, was etched with caustic and acid etchants, revealing dislocations at the orthoclase matrix interface with the twinned albite perthite, (Figure 5). Very thin sheets of albite perthites were extracted from mechanically polished and etched orthoclase during plastic replication for electron microscopy studies. Transmission electron micrographs were obtained revealing clearly the twinning structure of the albite perthite, (Figure 2).

Because the high density of exsolution dislocations at the microperthite boundaries, oriented crystallographically in orthoclase (Grossman and Wegner 1968), and the deeply etched microcracks in the orthoclase obscured defects and strains possibly associated with cleavage, a study was conducted to find slower etchants, which hopefully would aid in differentiation of various types of dislocations and their sources. It was found that hydrofluosilicic and hydrofluoroboric acid containing etchants resolved the problem for the (001) plane of orthoclase and also revealed more detail on the (010) plane. These etches revealed dislocation etch pits along the perthite-orthoclase matrix and within the perthites. Deep microcracks, which normally appeared after a 5 to 10 second etch with rapid HF etchants, appeared as a series of etch pits across the perthites which continued in a straight line into the orthoclase matrix (Figure 6). The other interesting features found were

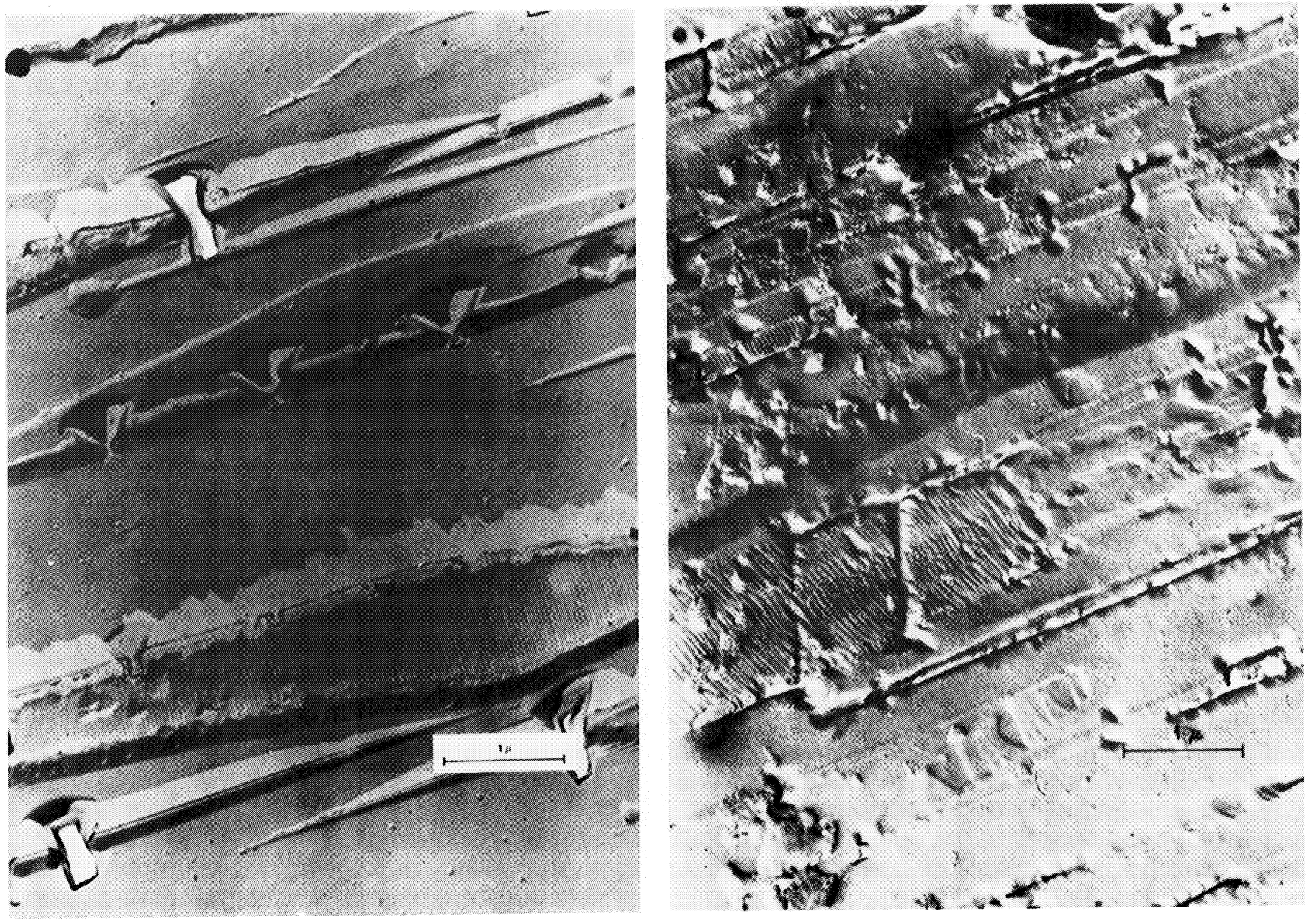

Figure 5. Dislocations at Microperthite Boundaries of Orthoclase (001) and (010)

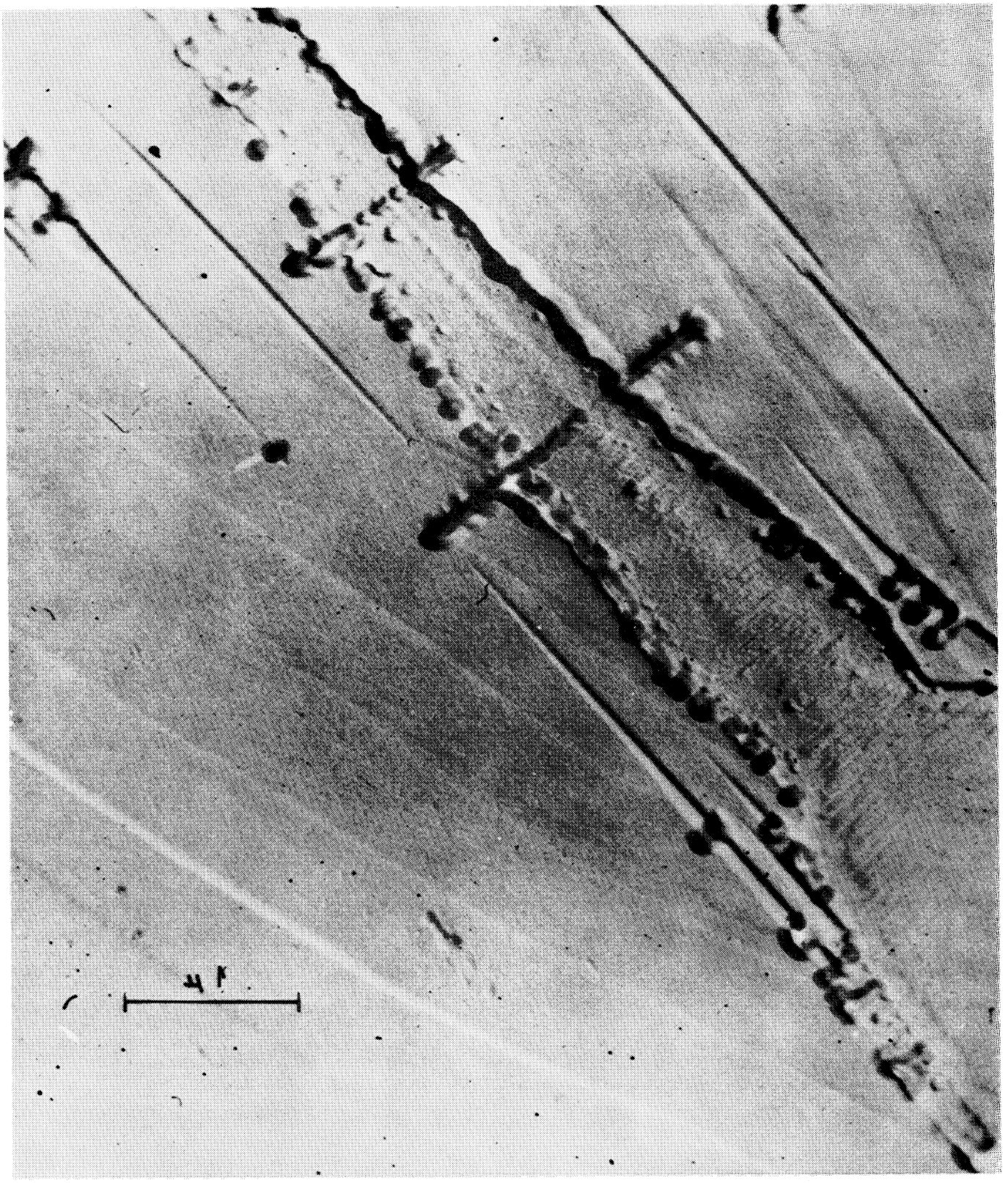

Figure 6. Microcracks Crossing Perthite Boundary into Orthoclase Matrix (001)

long narrow perthites (or another crystalline phase) with dislocation etch pits symmetrically opposed at the matrix interface, sometimes disconnected (thus not giving the appearance of a microcrack). Positive replicas were made of these surfaces for electron microscopy.

Albite (Na Al Si_3 O_8), an air cleaved crystal, polysynthetically twinned, was etched using the (1:1:1) HF, HCl, citric acid etchant. Large symmetrical pits resulted at dislocations on twin boundaries, the twin valleys showing smaller pits, Figure 7. The alternate pit shape on hills and valleys of albite twins is a characteristic feature found also on naturally deformed albite. This albite, exhibiting deformation bands (Figure 8), was probably shock deformed as evidenced by displacement and disruption of the deformation bands, accompanied by numerous dislocations, subgrain boundaries near fractures, polygonized dislocations and traces of slip planes crossing earlier twinning bands. Etching with a more dilute etchant (1:1:8) HF, HCl, H_2O also revealed what appeared as antiphase boundaries (Figure 9), which have been reported previously by McConnell and Fleet 1963.

Thin sections of albite showed dislocation structures in electron transmission (Figure 3). The chemical composition of this albite (from Amelia, Virginia) was checked by electron microprobe X-ray analysis, and showed an almost pure sodium alumino-silicate composition.

An albite crystal from Madagascar, etched on three low index faces: (001), (010), and (100) simultaneously, revealed different etch rates on all three faces; the fastest etching one was (010), then (001) followed by (100).

Diopside, Ca Mg $(SiO_3)_2$, a monoclinic silicate belonging to the pyroxene group of silicates, was air-cleaved and etched for 60 hours with (1:1:4) HF, HCl, HOAc. Figure 10a shows background etching, revealing the crystallographic structure and dislocation etch pits. Figure 10b shows a different area on the same crystal with rows of polygonized edge dislocation etch pits.

Hypersthene, (MgFe) (SiO_3), an orthorhombic pyroxene, presented more difficulties in etching. The HCl component in the etchant was replaced with

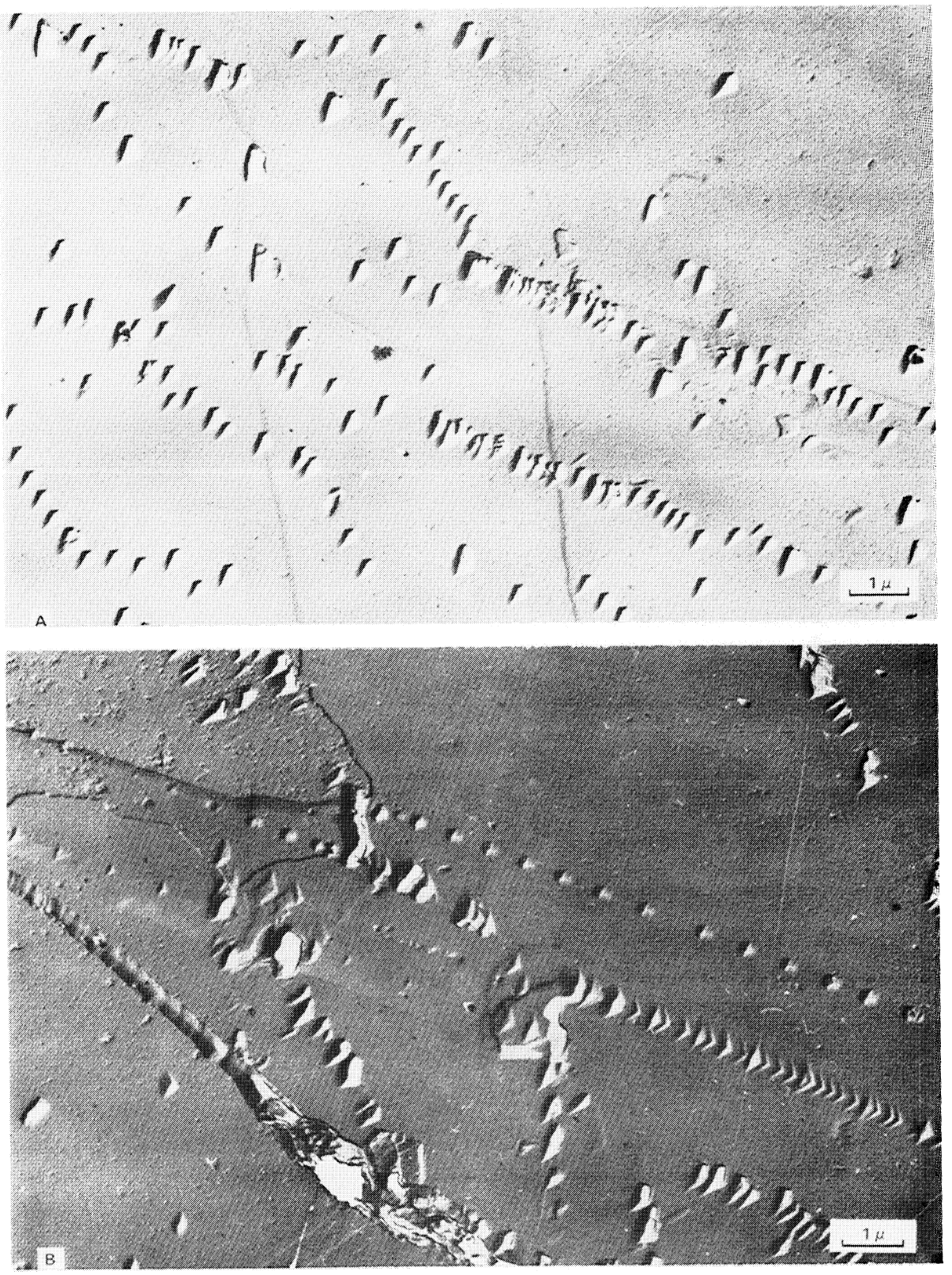

Figure 7. Albite (001), (a) Polygonized Dislocations, (b) A Twin Band Displaced Laterally by an Irregular Deformation Slip Plane

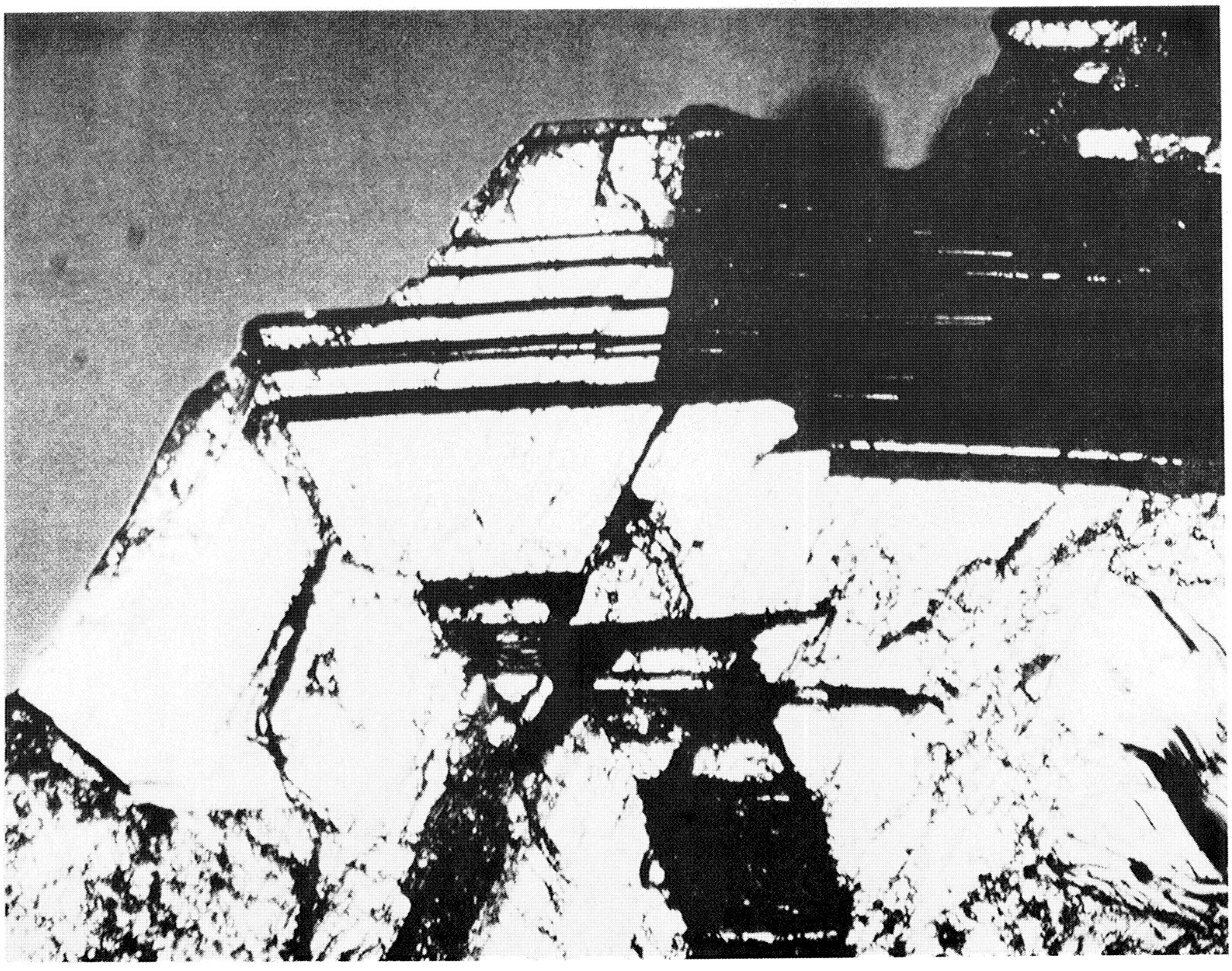

Figure 8. Albite (001) Deformation Bands. Same Crystal as Figure 7 at Lower Magnification

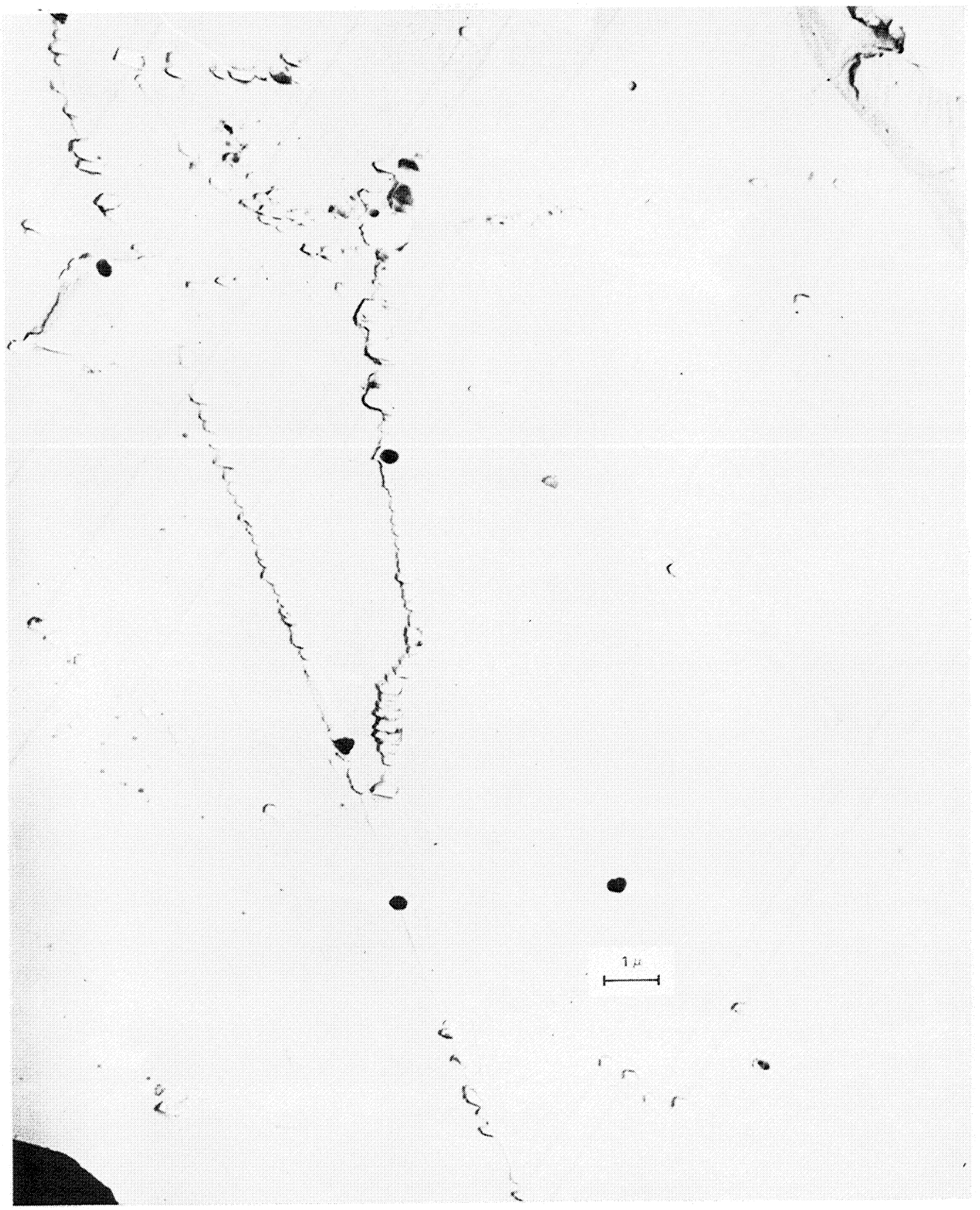

Figure 9. Albite (001), Etched Antiphase Boundaries

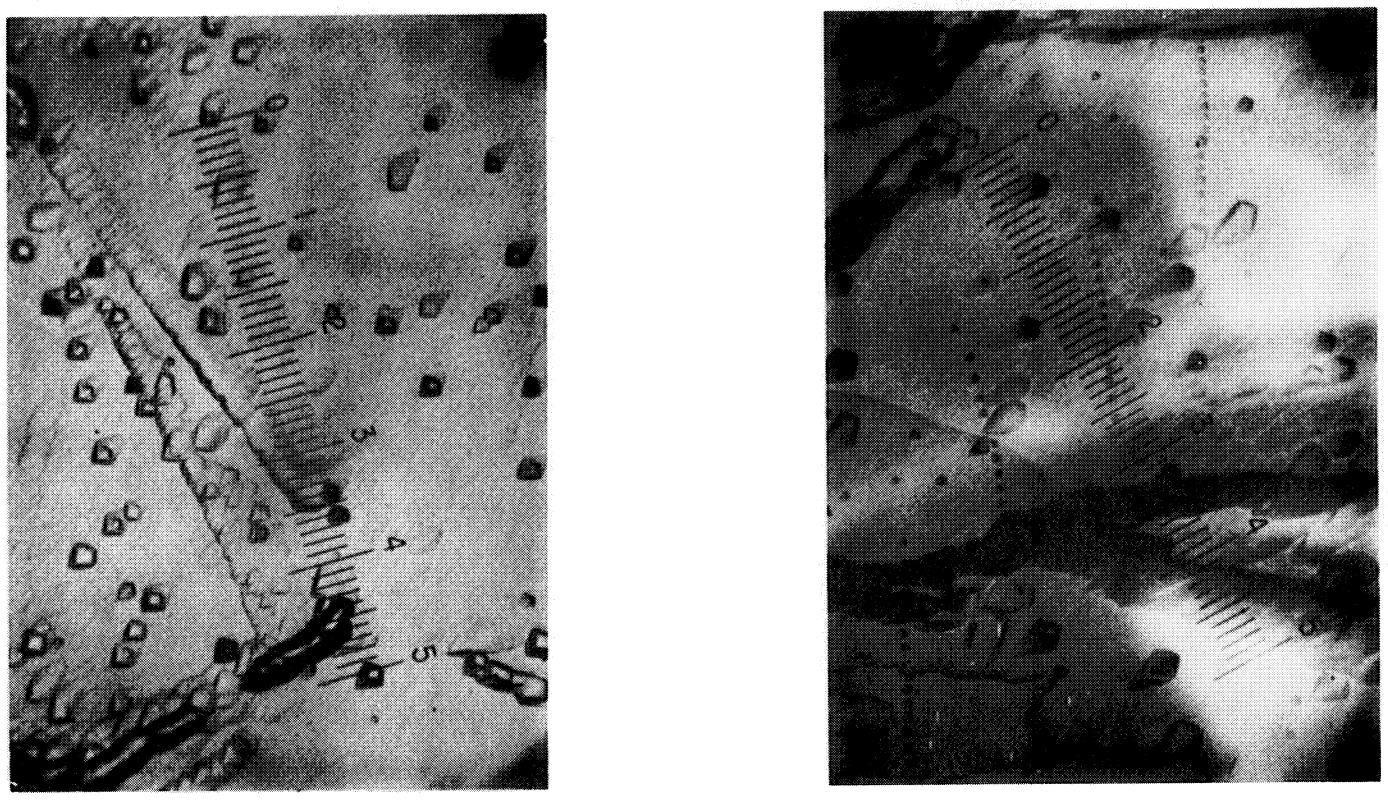

Figure 10. Diopside (100). (a) Quadrilateral Etch Figures with Mirror Symmetry, (b) Polygonized Etch Figures

HNO_3 to solubilize the Mg ion etching product (Figure 11a). Figure 11b shows a polished (100) surface after 10 minutes of etching.

Olivine $(Mg\ Fe)_2\ (SiO_4)$, an orthorhombic silicate, consists of independent SiO_4 tetrahedra. Dissolution with acids of a mechanically polished olivine crystal leaves an amorphous film of SiO_2 on the surface, which promotes a dendritic growth of impurity crystalline products. It was found that using the dislocation etchant (1:1:1) HF, HCl, citric acid, and boiling for 5 minutes in 20% citric acid, the surface film was dissolved, revealing dislocation etch pit arrays and subgrain boundary lines, consisting of polygonized dislocations.

A naturally deformed single crystal olivine, (Fo-Fa, 85%--15%), was encapsulated, polished, and selectively etched on the (010) plane. The orientation was checked by X-ray diffraction. Low angle tilt boundaries (Figure 12) are found together with slip planes, mostly parallel to the (100) plane but with a few parallel to the (001) plane (Figure 13). Numerous dislocation etch pits, polygonized edge dislocations (Figure 14) and dislocation pileups were observed (Figure 15). Repeated polishing and etching (six times), allowed tracing the dislocation lines and slip planes through the crystal (Figure 1.).

Another olivine crystal was X-ray oriented, cut and polished on the three orthogonal crystal planes: (010), (001) and (100). Deformation boundaries and dislocation etch pits were found on all three faces, differing in size and orientation dependent on the crystal orientation.

Biotite Mica was cleaved and etched with the (1:1:1) HF, HCl, Citric Acid etchant. Dislocation etch pits, local defect pits and radiation damage tracks were revealed simultaneously. The characteristic burst pattern of fission tracks in the etched mica is shown in Figure 16.

Calcium Fluoride, CaF_2, a model crystal, was chosen for etching study. Matching sections of freshly air-cleaved calcium fluoride, (111) oriented, were etched sinultaneously, revealing dislocations, polygonization, and subgrain boundaries. There was a one-to-one correspondence of the etch pits and boundary structures on the matching faces, confirming the selectivity

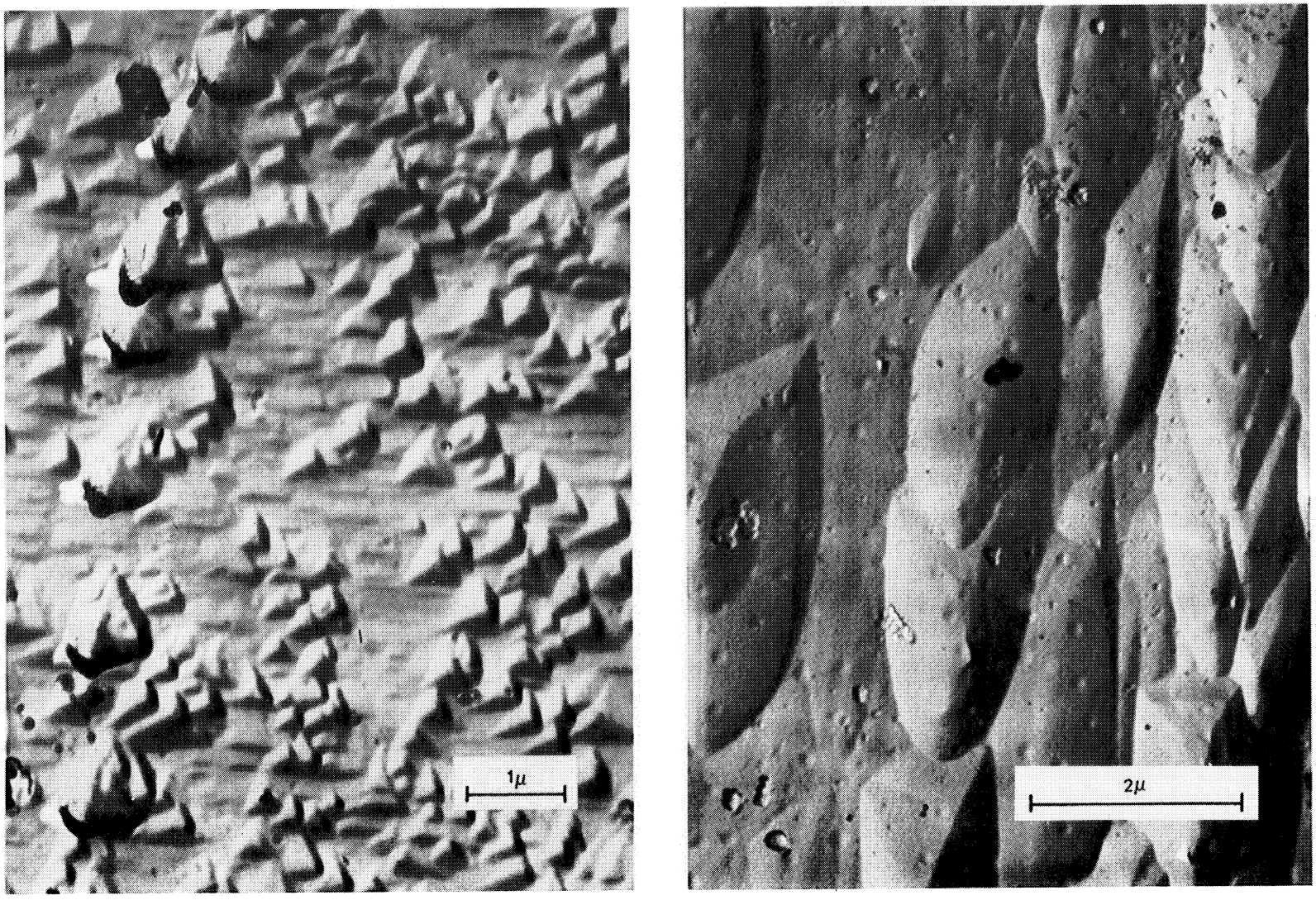

Figure 11. Hypersthene (a) (111) Face Etched with HF, HNO_3, HOAc, (1:1:4), (b) (100) Face Etched with Concentrated HF

Figure 12. Low Angle <100> Tilt Boundaries on (010) Olivine

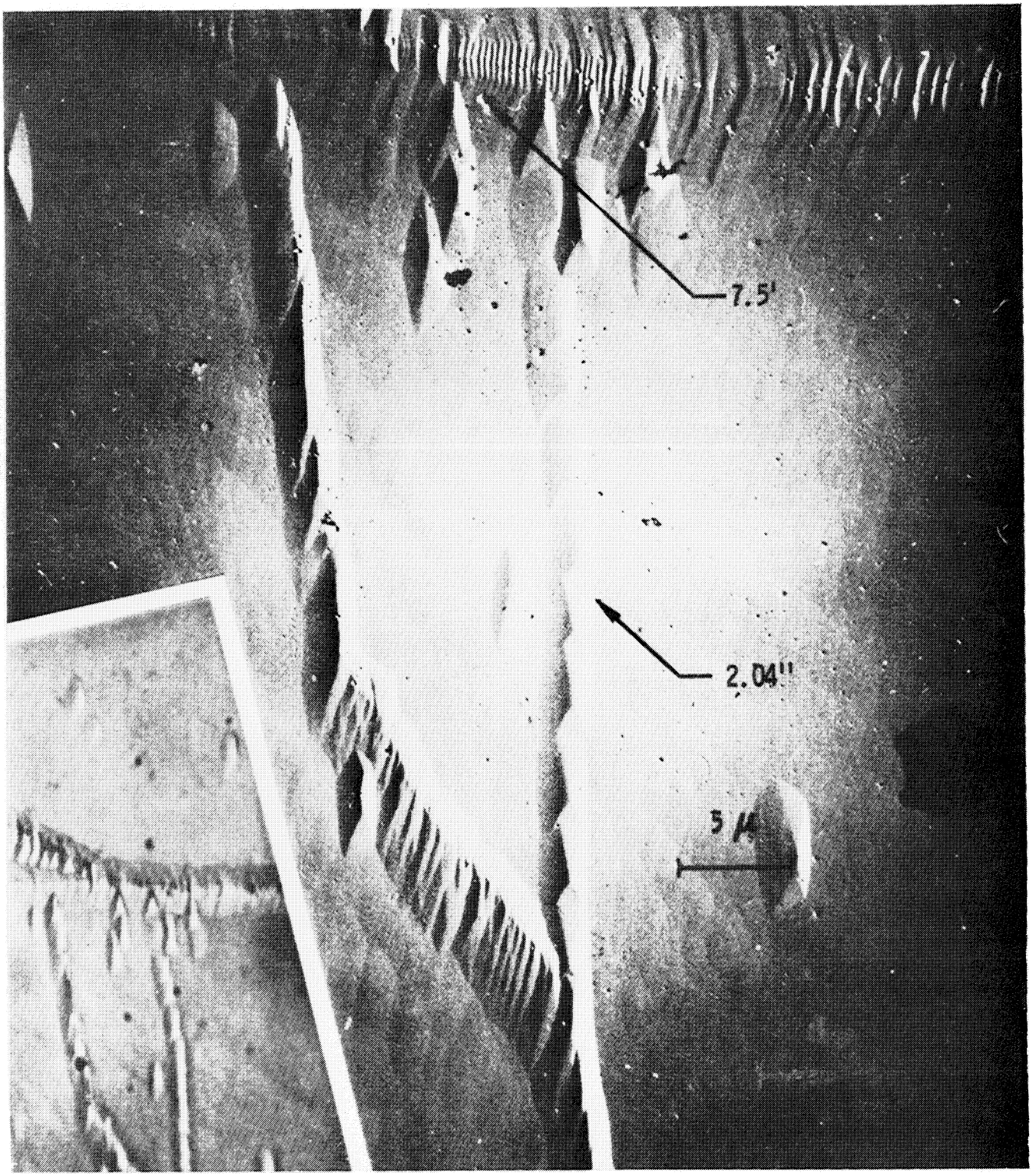

Figure 13. Very Low Angle <100> Tilt Boundaries on (010) Olivine

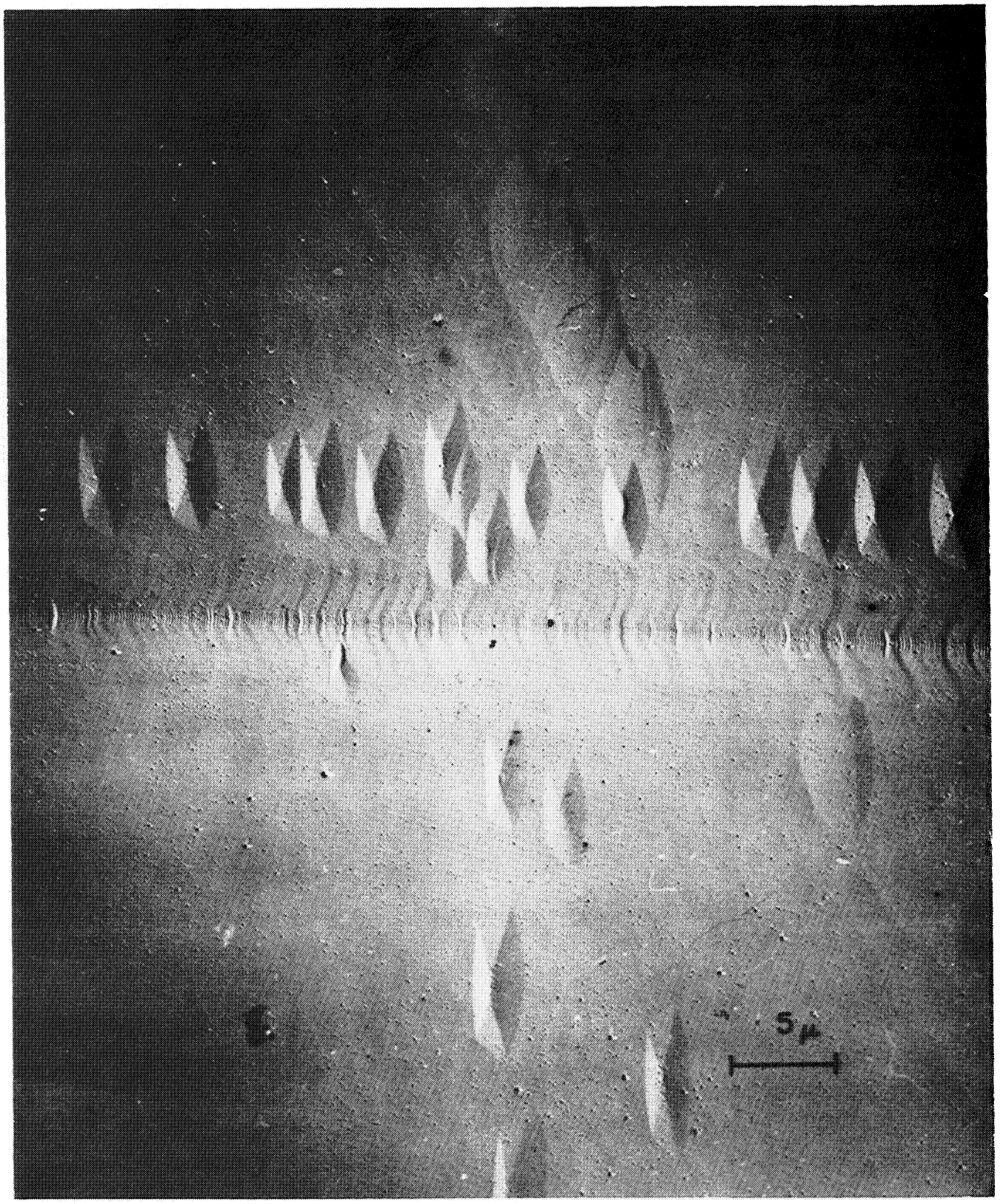

Figure 14. Polygonized Dislocations Adjacent to a Low Angle <100> Boundary on (010) Olivine

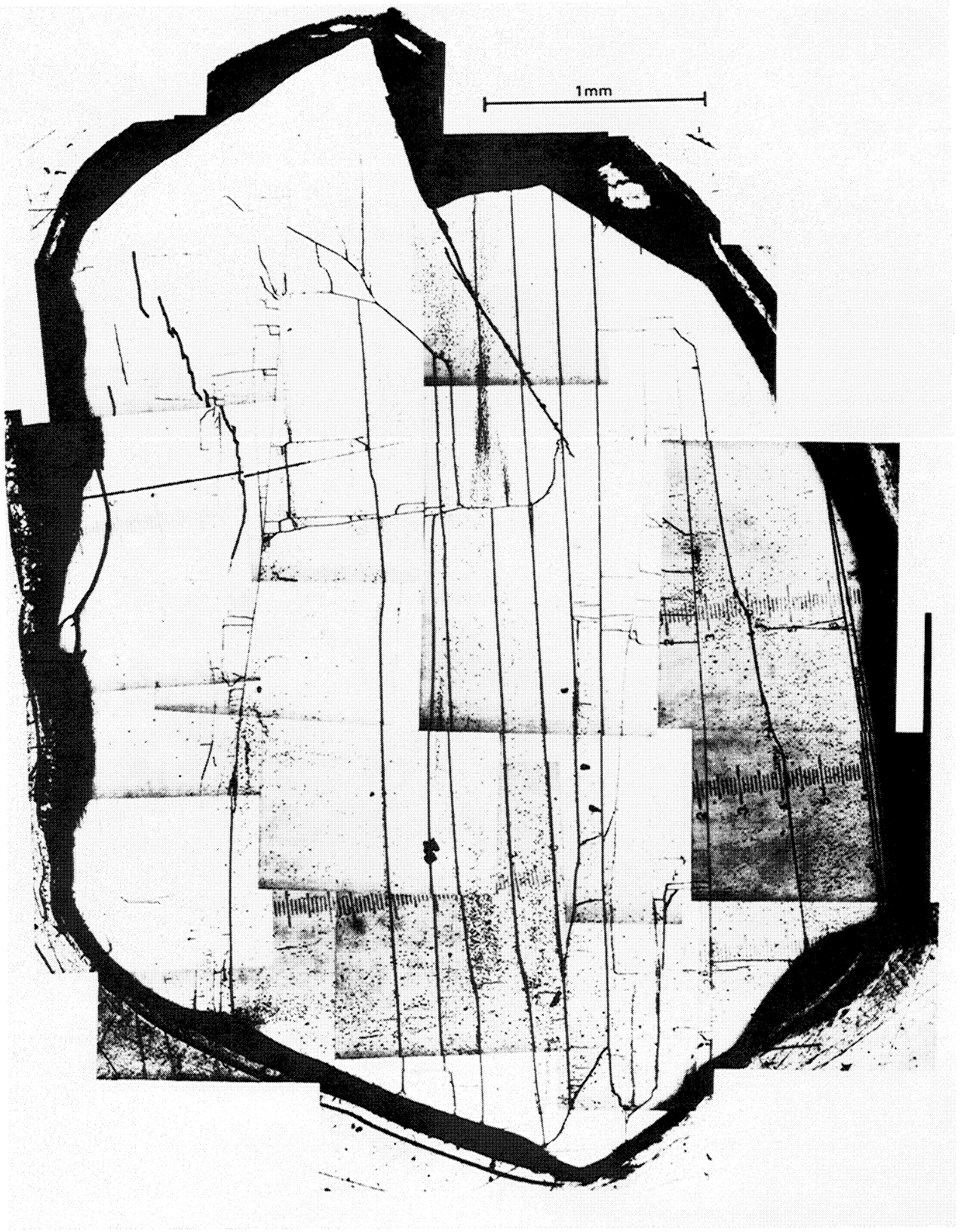

Figure 15. Olivine (001), Etched

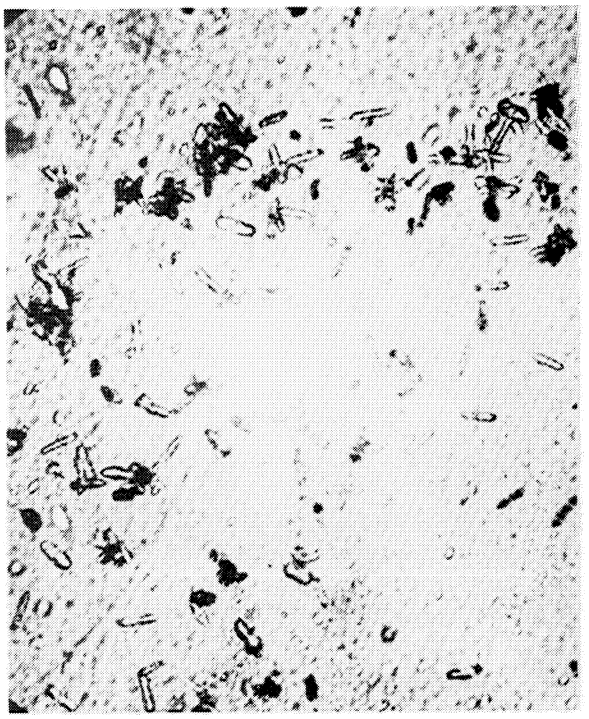

MAGN. 50X

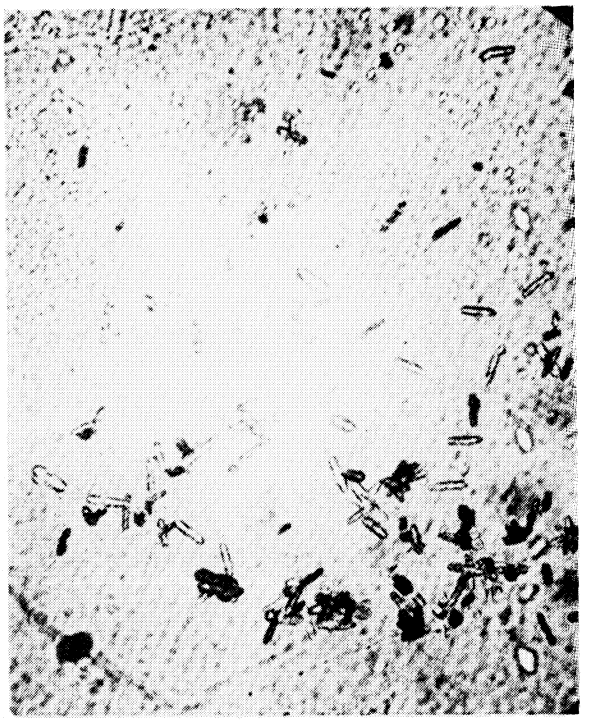

MAGN. 50X

MAGN. 70X

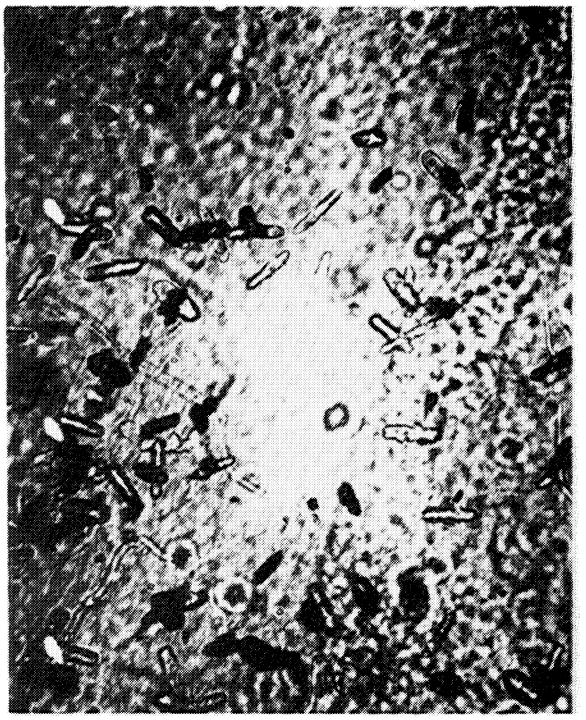

MAGN. 70X

Figure 16. Fission Tracks in Etched Biotite Mica Magnification

of the etchant (Figure 4). The etchant was a solution of ammonium chloride, citric acid and zinc chloride, used at 85° to 95°C for 10 minutes. The concentrations of the constituents of the etchant were varied, and all proved equally effective. The limits of the optimum concentrations have not as yet been established.

Vacuum cleaved (111) sections of calcium fluoride, whose electrostatic charge had been measured in ultrahigh vacuum, were chemically etched and metallized, and then the etch patterns mapped in utilizing an optical microscope. Results of etching the cleaved section are illustrated in Figures 17 and 18. The corresponding charge pattern is shown in Figure 19.

Some strongly shocked materials from the Nevada test site were subjected to selective etching. Very heavy fracturing and random orientation of various species of crystallites presented problems due to difference in reactivity of the different mineral species. Although mineral identification aids in selecting an optimum set of etchants and the order they are to be used, shock vitrified or disordered lattices cannot be expected to yield etch figures when the original crystal lattice is lost or the spacing between dislocations is less than the smallest resolvable etch figure. For less heavily shocked materials the maximum resolvable etch figure density using an optical microscope is approximately 10^{10} cm^{-1} and using electron photomicrographs of surface replicas, it is approximately 10^{14} cm^{-1}.

3.2 ELECTROSTATIC CHARGING

3.2.1 Run No. E-9, Albite (001)

An albite crystal was mounted, and the pressure was 7×10^{-11} torr after bake-out. The first attempt to cleave the crystal chipped a fragment from the cleavage notch. Pressure bursts in the high 10^{-9} torr range were observed. The second attempt was successful, and the crystal showed a dipolar distribution oriented parallel to the notch. The negative peak was 90 degrees clockwise from the chisel direction with a corresponding positive peak 173 degrees clockwise from the negative peak. The dipole peak to valley difference decreased monotonically to one-fifth its initial value in 13 days at which time the run was terminated.

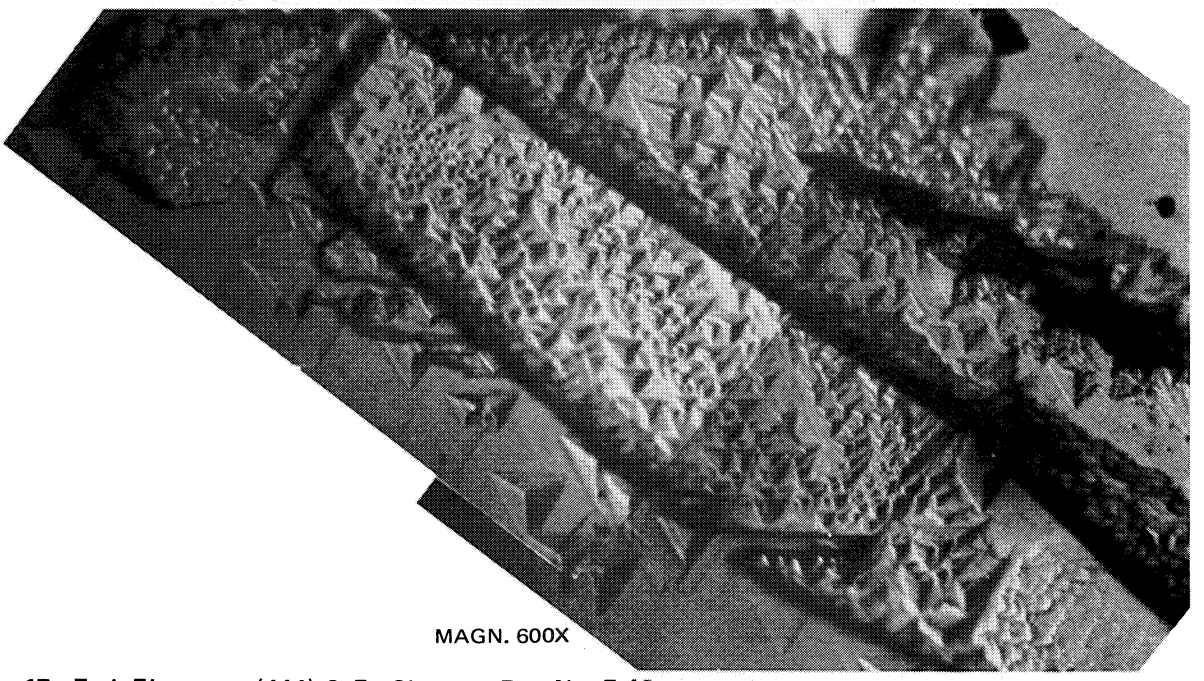

Figure 17. Etch Figures on (111) CaF_2 Cleavage, Run No. E-13. (a) Deformation from Knife and Anvil Cleavage. (b) Dislocation Pileup at Fault Located in Same Area as the Positive Peak Shown in Figure 18

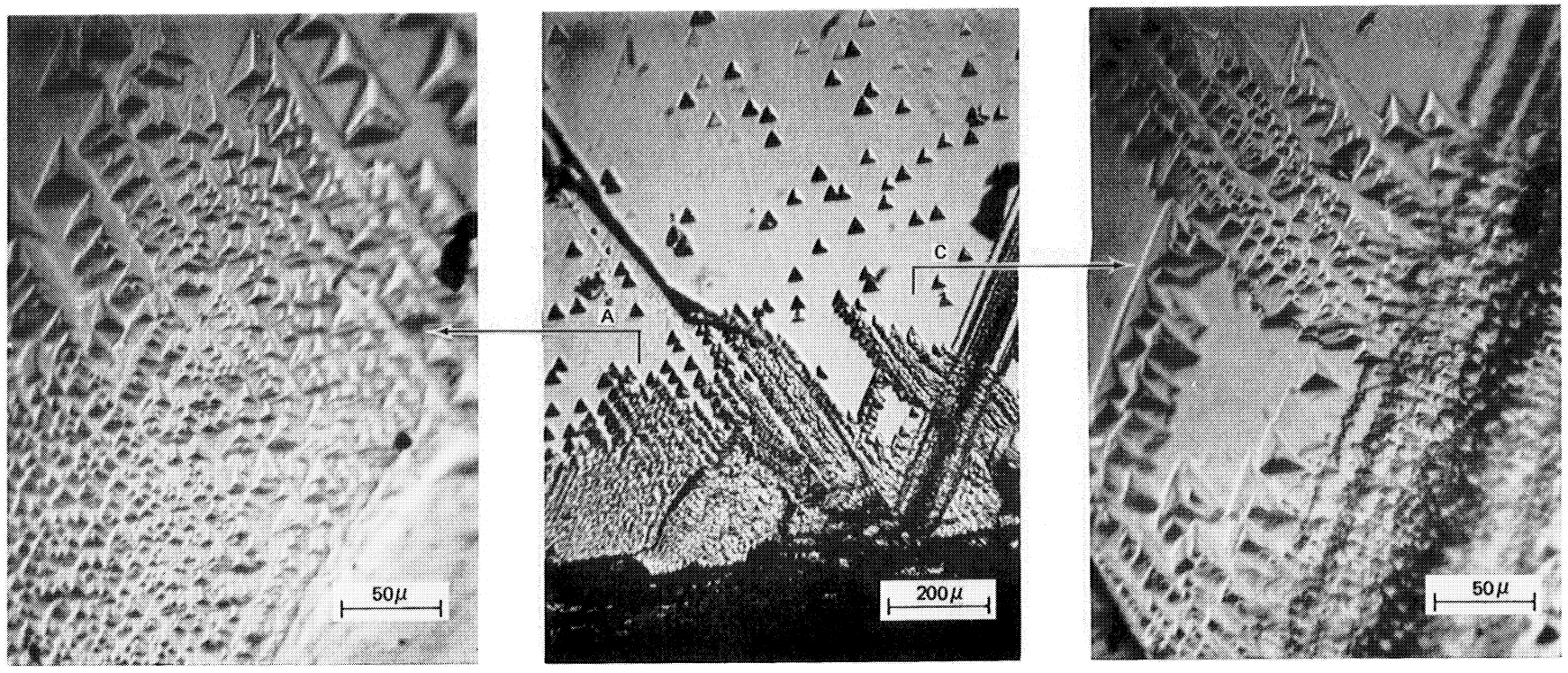

Figure 18. Photomicrographs of Defects due to Knife During (111) CaF_2 Cleavage Run No. E-13

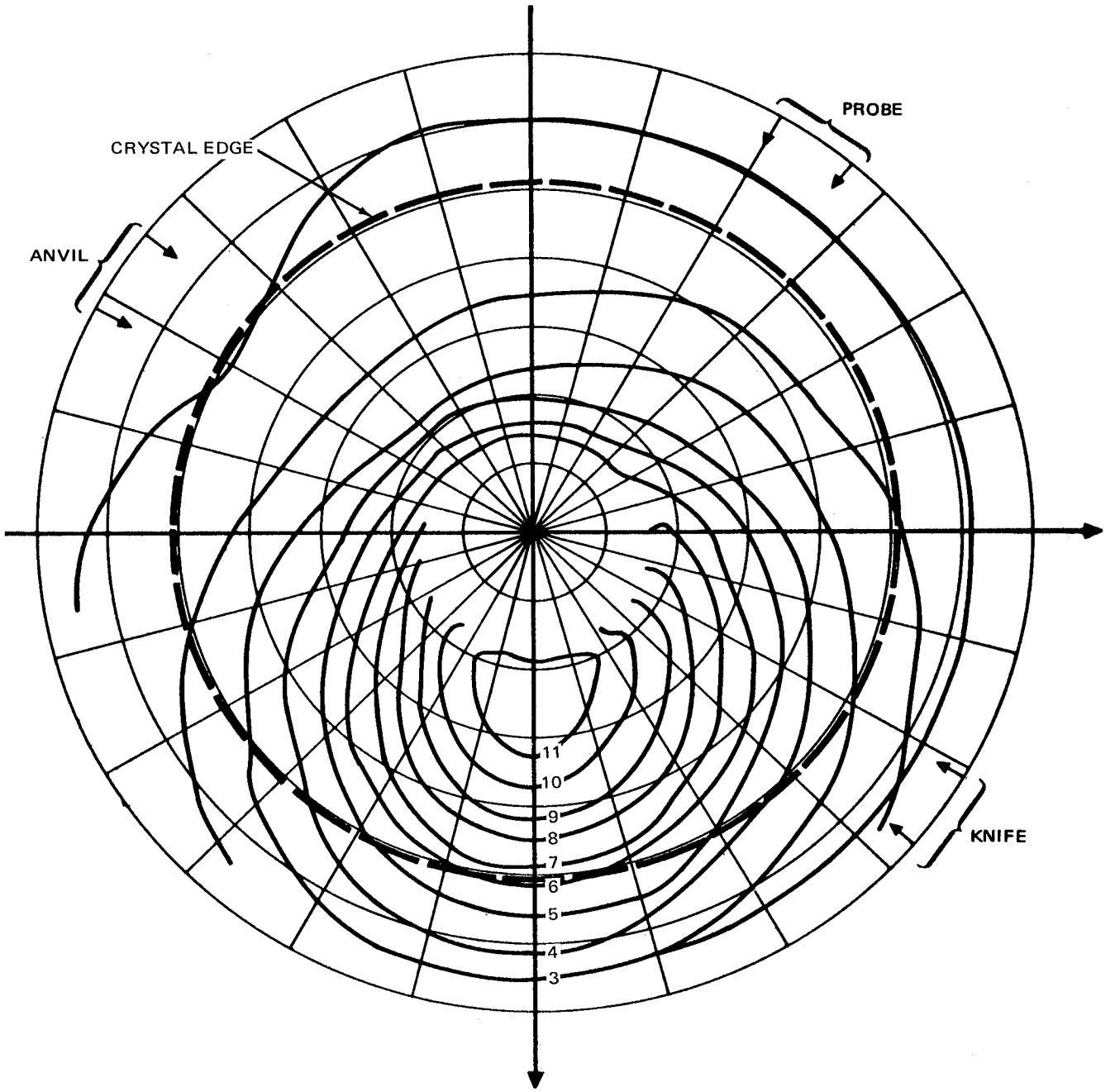

Figure 19. Electrostatic Charge Isodensity Distribution on (111) Cleaved CaF_2 Crystal, Run No. E-13

3.2.2 Run No. E-10, Albite (001)

The same albite crystal as used in Run No. E-9 was cleaved a second time without breaking vacuum. Pressure bursts in the high 10^{-9} torr range were observed again. It took 3 minutes to pump down to 1×10^{-9} torr and another minute to reach 2×10^{-10}; the pressure finally dropped to the low 10^{-11} torr range in 2 days.

A set of concentric polar charge distribution traces were made, and the dipole strength became larger as the electrometer probe moved radially outward from the crystal edge. This is discussed in Section 4.2. The dipole orientation was approximately the same as the previous run with respect to the cleavage notch.

3.2.3 Run No. E-11 CaF_2 (111)

Pure CaF_2 was the first synthetic model dielectric material cleaved in our vacuum system. It is cubic, (Z = 4), space group Fm3m. It has a perfect (111) cleavage and slips on (100) planes in (110) directions. A cylinder was ultrasonically cut perpendicular to a (111) face of a sample from (Harshaw Chemical Company optical grade). A pressure burst was observed in the 10^{-9} torr range. The charge distribution became erratic after 15 minutes, apparently when the crystal spontaneously fractured inside its retaining collar. At first, electrostatic and mechanical forces held the crystal fixed. However, after 24 hours, it became apparent that the crystal was moving far enough up and down in the collar that one edge was periodically contacting the probe during each revolution. This destroyed the gold guard-plane film on the glass, and the run was terminated.

3.2.4 Run No. E-12 CaF_2 (111)

A new razor blade and anvil described in Section 2.2 was used and the cleavage was significantly improved. The pressure rose to the high 10^{-9} torr range. Typical brittle fracture river patterns radiated from the knife edge toward the massively deformed counter-supported area resting against the anvil. The rationale that no sharp edge on the new anvil would ever touch the crystal due to misalignment and initiate a cleavage crack was verified.

The decay of the initially symmetrical peak is shown in Figure 20. A strong negative peak was located in the anvil area which persisted throughout the decay time period. At the end of 40 minutes, the electrometer probe to crystal surface distance was decreased to one-sixth the original distance and the peak valley charge difference increased by a factor of 10.5. This can be accounted for by the appearance of a resolved, secondary positive-going cleavage stress feature. When only the chisel-anvil charge difference is considered the charge increase is six because of the change in the probe distance. This is the expected value since at constant charge in the dielectric, the guarded electrometer probe should indicate a charge difference change which is inversely proportional to the probe-surface distance.

The run was terminated when the electrometer probe inadvertently touched the cleaved surface while attempting to make radial charge distribution measurements to obtain an isocharge density map.

3.2.5 Run No. E-15 CaF_2 (111)

After redepositing gold on the electrometer probe guard electrode, the same CaF_2 crystal as used in E-12 was cleaved again. A pressure burst of 10^{-8} torr was observed during the cleavage which very slowly decreased with time. The charge decay curve is shown in Figure 20, and an isocharge distribution curve is shown in Figure 19. The charge distribution shows a broad negative peak at the anvil, no charge feature at the knife position but an oriented, triangular charge distribution oriented 60 degrees to the knife-anvil axis. Photographs of the etched surface of this crystal are shown in Figure 17. The triangular etch pits show the same orientation as the charge peak triangle. An etched feature is found at a point corresponding to the positive charge peak as noted earlier. The magnified inset indicates that this is a fault region with dislocation pile up. Although most of the crystal growth dislocations are perpendicular to the cleavage plane over the surface of the crystal, (symmetrical triangular etch figures), there is a high density of isosoles triangular etch pits in the fault area.

3.2.6 Run No. E-14 LiF

LiF is a relatively plastic crystal at room temperature and when cleaved at 10^{-9} torr, exhibited a wide variation in peaks. Visually, each peak or

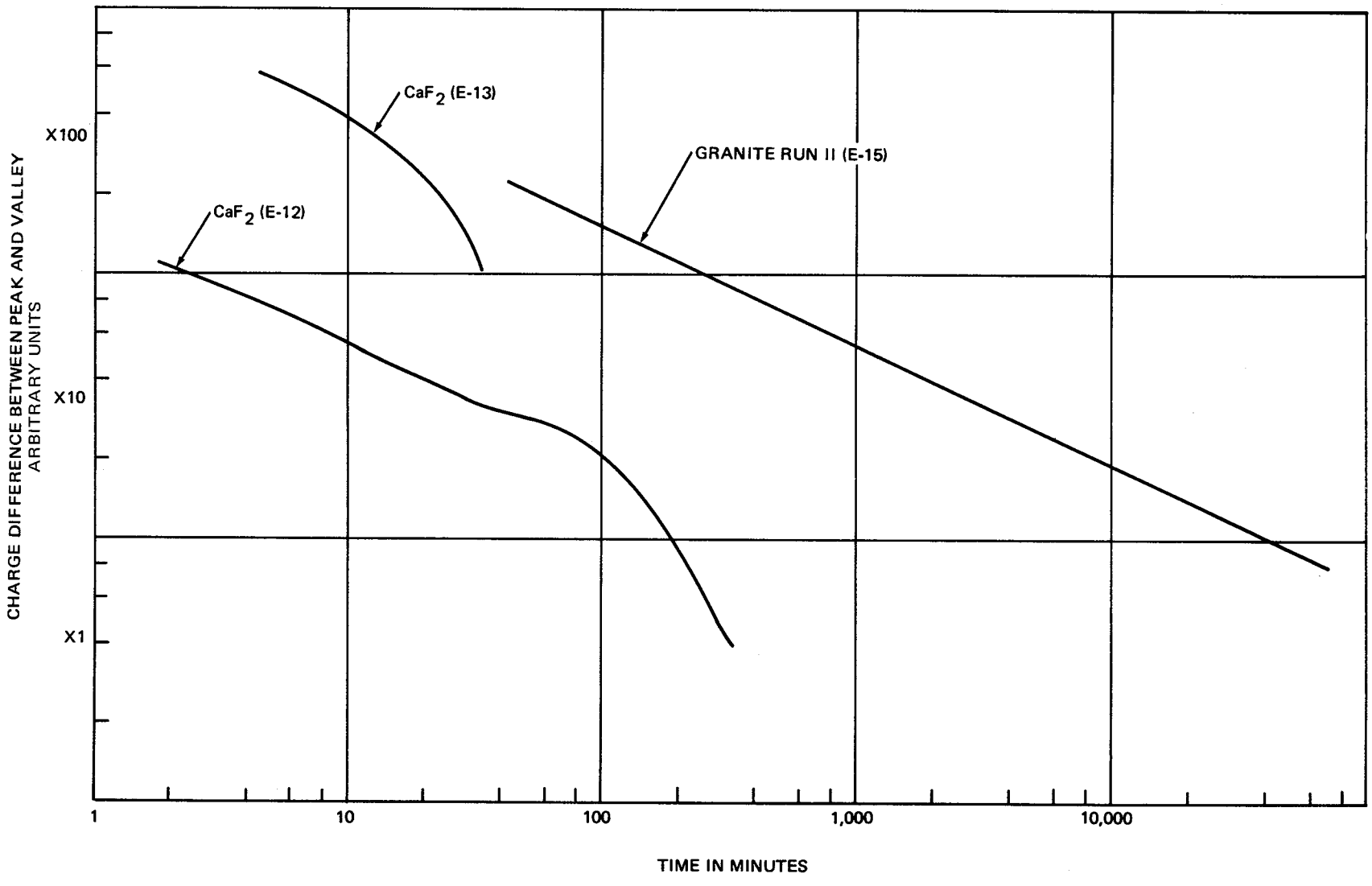

Figure 20. Variation in Peak to Valley Charge Difference with Time for CaF_2 and Granite Cleavages

valley was related to some type of deformational stress. The nine initial peaks and valleys were referenced to a peak near the knife. The sequence of peaks is shown in Figure 21 and their relative time variations are shown in Figure 22. Since the peaks I, II, III, and VI level off at +1 peak unit, peak IV, V, and VII level off at +2 peak units, and peak VIII and IX have shifted to the +5 peak unit level, it is clear on detailed study that the charge redistributes into three dominant peaks associated with the anvil, the knife and pressure point near the knife in the direction of a deformed area which are all optically active in polarized light. The time scale for charge redistribution is also the shortest observed thus far.

3.2.7 Run No. E-15 Granite

Cylinders were cut from a polycrystalline granite sample from Cripple Creek, Colorado. The grain sizes were larger than 2 to 3 mm. The dominant phases are feldspar, quartz, and at higher magnification 50μ size particles of mica can be seen distributed throughout the sample. It was notched in the usual way and when fractured a pressure burst was observed in the high 10^{-8} torr scale. A simple dipole peak structure was observed when the probe was held far from the surface due to the jagged fracture. The time dependence of the peak to valley charge difference is shown in Figure 20. It is the only case found where the charge decays by a simple power law: $\log Q = -2.19 \log t$.

After a sufficiently long decay time, an isodensity charge distribution plot was constructed from charge measurements at different radii. This is shown in Figure 23, together with a photograph showing some of the main features of the fracture. The highest positive density peak $Q = 11$ corresponds to the highest point P on the ridge H running from about 220 degrees at the edge toward the center. The ridge falls off onto a well-cleaved feldspar grain on the right and a conchoidally fractured grain on the left. The low point, $Q = 3$, at 100 degrees, corresponds to a stress point P1, formed by the confluence of the valley marked V (which traverses the entire crystal horizontally) and the outline of the quartz grain A, which also formed a subsidiary maximum $Q = 4.1+$. The flat area corresponding to the notch between 0 and 80 degrees shows a uniform charge density. The remaining electrical features, the $Q = 9.0$ ridge at 330 degrees, and the deformation of the isodensity charge

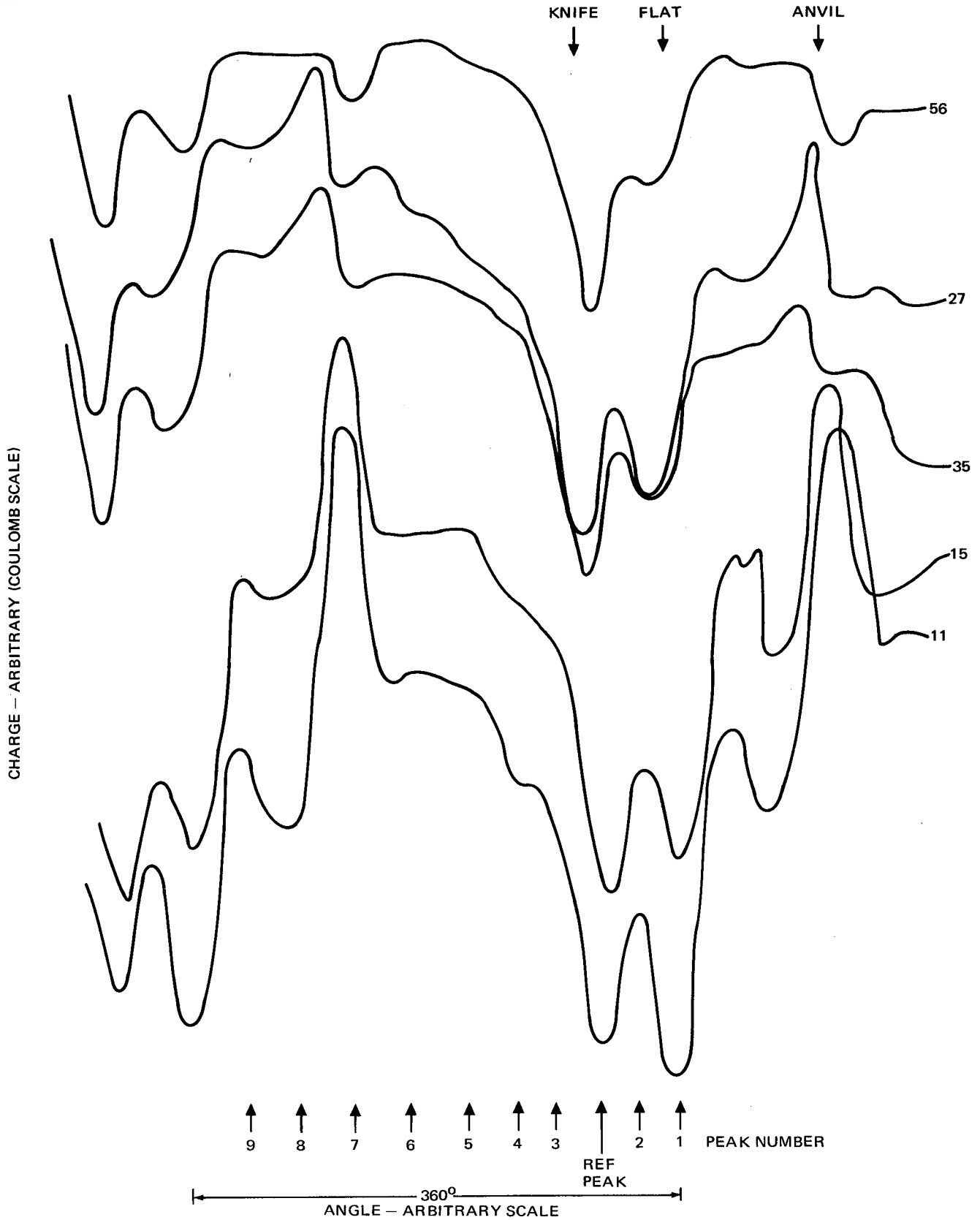

Figure 21. Variation in Charge Distributions with Angle for LiF Cleavage No. E-14 at a Series of Times After Cleavage

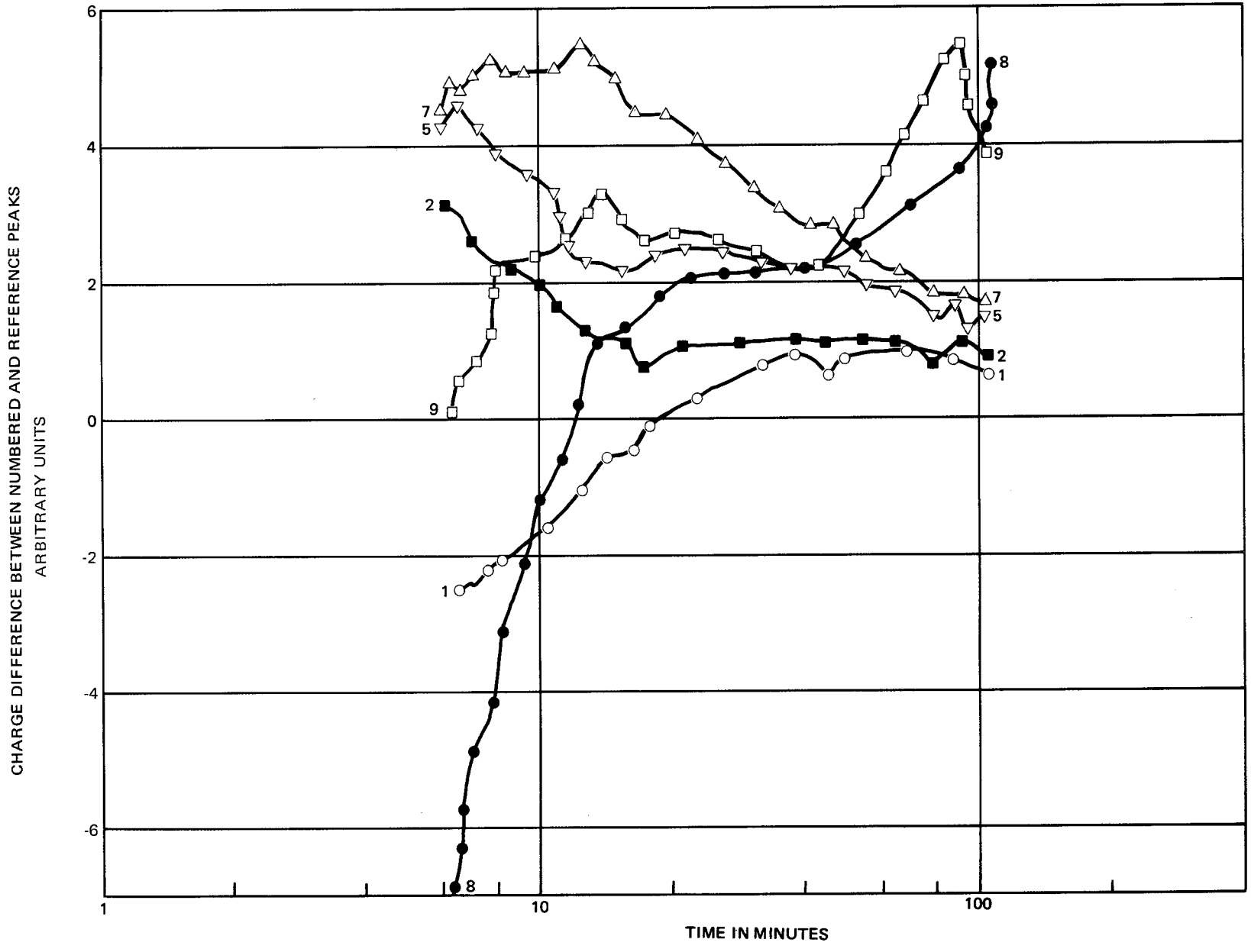

Figure 22. Variation with Time for LiF Peaks Run No. E-14. Peak Numbers are Identified in Figure 21

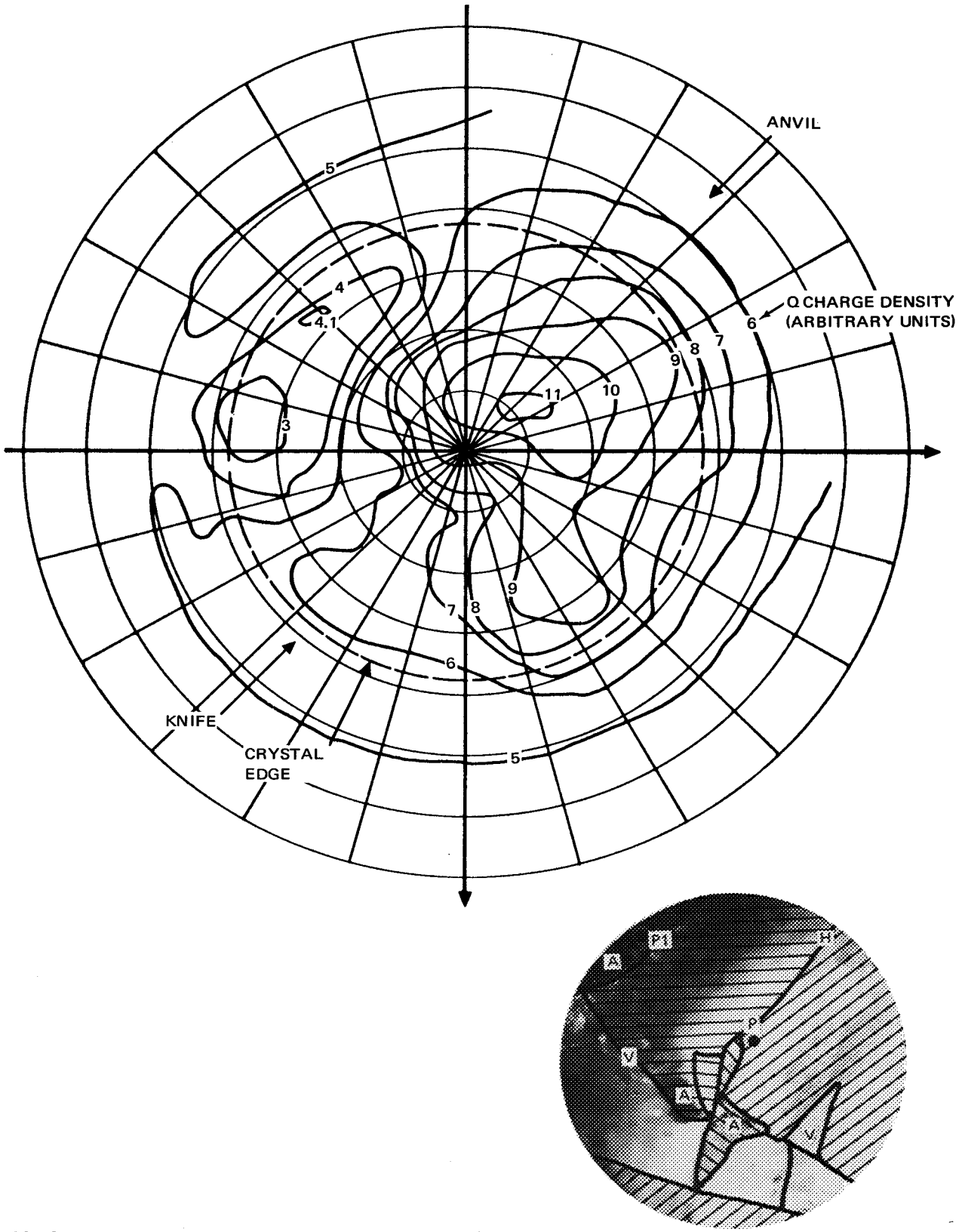

Figure 23. Charge Isodensity Distribution Curves for Granite Fracture Run No. E-15. Photomicrograph Insert Shows Topological Features

lines from 350 to 90 degrees near the crystal center appear to be associated with the exposed quartz A in the Valley V-V crossing the crystal.

3.3 SILICATE ADHESION

Orthoclase (001) and Aluminum Alloy (2024)

Results from the first day of this run were reported in the fourth year summary report. The run was completed during the present reporting period and is summarized here.

The system was evacuated to 3×10^{-10} torr and then backfilled with argon to 2×10^{-2} torr. The metal sample was sputtered for 45 minutes at 2 to 3 ma. The orthoclase was cleaved 12 minutes after completion of sputtering, at a system pressure of 1×10^{-7} torr. The cleavage surface was highly irregular. Contact was made with the metal sample 3 minutes later. An adhesion force of 1.8×10^{3} dynes was measured, and a strong long range attractive force was present. The adhesion force decreased to 1.2×10^{3} dynes at the end of an hour and continued to decrease slowly during the next 78 days at which point the run was terminated. The adhesion force at that time was 6×10^{2} dynes. This run demonstrates experimentally the expected persistence of the charge for long periods.

Basalt (Lintz-Rhenish, Prussia)

This rock was quite fine grained, individual crystallites being a few tens of microns in diameter and less. The system was evacuated to 6×10^{-10} torr and the basalt fractured. Contact was made 9 minutes later. No adhesion force would be measured, indicating that whatever was present was less than 1×10^{2} dynes. Several small particles produced during fracture were noted to align themselves with their long axis perpendicular to the lower fracture surface. This indicated the presence of electrostatic charging, but of a magnitude much smaller than had been observed previously for single crystal minerals.

The basalt was then re-fractured and contact made two minutes later. A single value of 3×10^{2} dynes was obtained for the adhesion force. The force dropped below detectable prior to the next contact one minute later. This single measurement could be erroneous since fracture occurred within the

sample holder and it is hence not certain whether sample contact had actually been made.

Diabase (Topanga Canyon, California)

This rock was more coarsely grained than the basalt, with a few crystallites as large as 1 mm. Fracture was accomplished at a system pressure of 4×10^{-10} torr. No measurable adhesion was present. A few small particles produced during fracture were, however, noted to attach themselves to the chisel.

Anorthosite (Norway)

This rock contained a number of crystallites of size 1 mm or larger. Three fractures were made, all at 2×10^{-10} torr. For the first, contact was made five minutes later; for the second, 16 minutes later, and for the third, 21 minutes later. No measurable adhesion was present.

Granite (Cripple Creek, Colorado)

This rock consisted primarily of grains of size 1 to 2 mm with many being several millimeters. Two fractures were made; the first at 3×10^{-10} and the second at 2×10^{-10} torr. Initial contact for the former occurred eight minutes after fracture; for the latter, 10 minutes after fracture. No measurable adhesion was present for the first run. However, it was noted that several small flakes jumped from the lower to upper sample as the samples were being brought toward contact. For the second, measurable adhesion was present. The initial measurement gave an adhesion force of 2×10^{2} dynes. This remained relatively constant over the next 10 minutes, but thereafter decreased slowly and 6 hours later was below measurement capabilities ($<1 \times 10^{2}$ dynes).

Section 4
DISCUSSION

4.1 CHEMICAL ETCHING

The chemical etch-pit method has proven successful in bringing out defects in the crystal structure of silicate minerals and ionic crystals. The presence and distribution of dislocations originating from crystal growth or caused by cleavage as evidenced by etch pits, has aided in the interpretation of electric charges on cleaved crystal surfaces and the understanding of adhesion phenomena.

The selective etching of natural silicate crystals has been found to be dependent on many factors of chemical composition, crystalline structure, and the presence of impurities, which change the solubility rate of the species and may also act as inhibitors or poisons enhancing the selectivity of the etchant at dislocation sites. The most useful etchants reported here are mixtures of (1) HF + HCl + Citric Acid; (2) H_2 SiF_6 + HCl + Citric Acid; (3) HF + HNO_3, and (4) HF + HCl + H_2O. The dislocation etchants have also been shown useful for fission track etching in micas and plagioclases and, as found from the Apollo 11 lunar samples, for pyroxenes. The structural features brought out by etching were growth defects, twinning, exsolution bands, variations in crystalline phases, and plastic and shock deformation. The sequence of forces acting upon the crystal can be deduced from the etch-pit features.

Two significant advances in selective etching of silicate crystals have been achieved. One of them is a method for dislocation etching on the (001) and (100) faces of naturally deformed crystals of olivine (Wegner and Grossman 1969), the second is improved dislocation etching of feldspars, and revealing crystal structure defects in orthoclase and albite by transmission electron microscopy, and replication of adjacent areas.

Of the possible lunar materials, titanium containing rocks were studied, but methods of selective etching have not yet been perfected. Ilmenite ($FeTiO_3$) and sphene $CaTiSiO_5$ single crystals have been obtained to facilitate the etch-pit study. We have found, in conjunction with the analysis of Apollo 11 Lunar materials, that ilmenite etches preferentially along with the pyroxenes (Grossman, et al, 1970).

Preparation of the mineral species for etching created many problems. Suitable encapsulation and polishing methods vary with crystal orientation because of the hardness anisotropy and preferential cleavage directions for various crystal structures. Where possible, cleaved crystals were used for dislocation etching studies.

The methods developed for defect etching of terrestrial silicates have been adapted successfully for the analysis of lunar materials.

4.2 ELECTROSTATIC CHARGING

A significant result with two cleavages in the same direction in the same albite crystal is that the dipole orientation is the same in both cases (runs E-9 and E-10). This verified the orthoclase cleavage results (runs E-5 and E-6) where a charge orientation was first observed to be related to cleavage direction. On the other hand, the strain induced charge localization opposite the cleavage point was not observed as markedly as in orthoclase. Instead, the charge distribution is more of a symmetrical dipole where charge localization, if it occurred, rapidly redistributed.

Another important similarity between the orthoclase and albite experiments is that the net charge density difference of the second cleavage is larger than the first. On the other hand, there is a marked increase in the dipole field as the probe moves to radii larger than the crystal diameter with albite, the exact opposite to the orthoclase crystal where charge localization is observed. One possible explanation for the differences in the two materials is that the conductivity of albite is greater than orthoclase. Another possibility is that the albite is exhibiting a precleavage polarization.

The CaF_2 model material cleavages E-11 to E-13 and the more ductile LiF cleavage E-14 have been particularly informative since crystal homogeneity and purity precluded internal polarization from composition gradients. This is conclusive experimental evidence that composition gradients, which might have but were never found to contribute to the silicate mineral cleavage charge distributions, are at most second order effects.

Residual charge density contours (taken after stabilization) on CaF_2 Run E-13, Figures 19 and 17 respectively, suggest that dislocation pileups around a crystalline defect area are charged. Dislocation slip systems which intersect the cleavage plane at an angle are assumed to be the most important in carrying the charge (i.e., those dislocations associated with isosceles triangular etch figures). In the other runs the anvil is a deformation point which dominates the charge. It should be emphasized that the model material cleavages produced charge distribution densities which were one to two orders of magnitude lower than the orthoclase crystals for which the local anvil stress was much more pronounced, the crystal resistivity very much higher and the crystal axis inclined to the cleavage plane.

Similarly, LiF shows a rapid decay in charge density due to its lower resistivity. The charge remains at regions which, on removal from the system, are still optically active.

The granite cleavage E-15, which has a low charge density is anisotropic and related to both the fracture topography and the exposed minerals. The jagged cleavage provides an anisotropic charge of low magnitude so that lack of observing the long-range adhesion force between complimentary segments is not surprising. When another granite crystal was carefully fractured (the run was terminated for a mechanical malfunction not related to the experiment and is not reported) the fractured section remained attached as has been observed with orthoclase cleavages. The crystal was separated, using the anvil to displace the fractured wafer sufficiently far that electrostatic repulsion of like-charged areas caused separation

The main factors which most likely contribute to producing electrostatic charging of ultrahigh vacuum cleaved or fractured materials are:

A. Stress deformation--dislocation motion
B. Triboelectric effect
C. Internal polarization fields
D. Possibly piezoelectric effects.

Unfortunately, we were unable to obtain suitable cores from ZnS and CdS, two piezoelectric crystals, which would be very interesting specimens on which to measure charge distributions particularly if conchoidally fractured perpendicular to the (111) piezoelectric axis.

Two spontaneous discharging processes have been found. First, a pressure dependent gas adsorption provides surface polarization which reduces the field external to the crystal. Secondly, bulk crystal conductivity permits charge dissipation at a slower rate, discharge times varying from half lives of 15 minutes in LiF to 75 days in orthoclase.

Discharge rates have been increased by crystal irradiation with low intensity UV for 24 hours. However, a recent analysis of the effect of solar UV on the moon (Appendix A) shows that with the high solar intensities it is possible to induce a stable electrostatic cohesion which exceeds Van der Waals forces.

4.3 SILICATE ADHESION

Adhesion studies during previous years, involving ultrahigh vacuum formation of the surfaces to be contacted, were directed toward single crystals having good cleavage directions. Cleavage rather than fracture was preferred since this resulted in a surface geometry more regular and controllable than that produced by fracture, and hence reduced both experimental and data interpretation difficulties.

Study of the adhesion of Apollo 11 lunar samples indicated, however, that study of fractured surfaces should be undertaken. Two reasons for this were that (1) the samples made available to us were rock fragments rather than single crystals, and (2) the results obtained were generally different

from those obtained for terrestrial single crystal minerals. The Apollo 11 results are summarized briefly below.

One chip each from Rocks No. 17 and No. 65 were received. Both are microbreccias. No. 65, in particular, is quite friable, requiring little force for disruption. No. 17 is significantly more competent. The first run was on No. 65, which was fractured at a system pressure of 7×10^{-10} torr. The first measurement gave an adhesion force of 8×10^{2} dynes. The force dropped to 2×10^{2} dynes after 4 minutes and shortly thereafter fell below measurement capabilities. Though this behavior was somewhat comparable to that found for the vacuum-cleaved single crystals, subsequent fractures of both 65 and 17 did not produce detectable adhesion. There were, however, indications of some electrostatic charging in that particles broken loose during fracture were often noted to align themselves with the samples as contact was approached Others would stand with their long axes perpendicular to the fractured surfaces.

The terrestrial rocks for study were chosen on the basis of their encompassing a large range of grain (crystallite) sizes. No adhesion was detected (except for the possibly spurious single measurement on basalt) until the second granite run. The reason for such behavior is not at present clear, but two possible explanations exist. First, it may well be that in cleavage the stress wave is channelled primarily along the cleavage plane, producing high stress concentration areas adjacent and opposite to the point of cleavage, and generating high charge concentrations (the relation between stress/strain, dislocation density, and charge concentration is discussed in Section 4.2). Fracture of polycrystalline materials, on the other hand, may well cause considerable scattering of the stress wave, thus spreading the stress over a much larger volume, thereby reducing the magnitude of the stress concentration. Second, the movement of dislocations is quite probably seriously impeded in polycrystalline materials by their being trapped within the various crystallites (e.g., they experience difficulty in crossing grain boundaries). This means that the areal extent of given charge concentrations would be determined to a significant degree by the crystallite size. If correct, this would indicate that for very fine grained rocks essentially perfect prefracture alignment must be attained for large adhesion to be developed, and

that this alignment requirement is considerably eased as the crystallite sizes become larger. The data obtained suggest that this may be the case.

In summary, further study is obviously required to determine the reason for the noted behavior of polycrystalline materials, but it appears at present that their adhesion magnitude depends importantly upon the path of the fracture, the crystallite size (and orientation), and the degree to which pre-fracture orientation can be achieved.

Section 5
SUMMARY

Studies were made during this reporting period to investigate: application of defect etching techniques to a variety of possible lunar silicates; the origin and stability of electrostatic charging produced by ultrahigh vacuum cleavage of silicates and model materials; and the adhesion of polycrystalline silicate rocks fractures at ultrahigh vacuum. Crystal defect etches for a suite of minerals were studied. Charge distributions on cleaved or fractured albite, CaF_2, LiF and granite were measured, using a guarded electrometer probe. Adhesion of polycrystalline rocks was studied using a rock suite of differing grain (crystallite) size. Replica electron microscopy and electron microprobe techniques were used to analyze surface features and mineral composition.

It was found that:

A. Selective etches depend on parameters such as solubility, common ion effects, ionic radii and complexing. Based on these considerations, specific etches were developed for a suite of silicates: orthoclase, albite, diopside, hypersthene, olivine and biotite mica. An etchant was also developed for CaF_2, a model material used for charge distribution measurements.

B. Measurements of charge distribution on cleaved albite, CaF_2 and LiF, and on fractured granite, indicated that the discharge rate varied directly with electrical conductivity, and that residual charges were centered around defect structures and stress deformed areas.

C. The main factors which contribute to producing the electrostatic charging are: stress deformation, triboelectric effect, internal polarization fields, and probably second-order piezoelectric effects.

D. The lack of consistent observation of long range electrostatic forces in fine grained terrestrial rock is related to a lower average charge

density compared to orthoclase, a more random distribution of charge centers, and non-planer fracture of the polycrystalline samples.

E. A theory is proposed that lunar adhesion is due to electrostatic charging stabilized by solar ultraviolet radiation (Appendix A).

Appendix A

LUNAR SOIL ADHESION DUE TO ELECTROSTATIC FORCES STABILIZED BY SOLAR RADIATION

by

Jack J. Grossman
McDonnell Douglas Astronautics Company--West
Huntington Beach, California

Choate, et al. (1969), and Scott and Roberson (1969) first observed, in the Surveyor III results that even though the lunar soil bearing strength was predominantly frictional, it had a cohesiveness sufficient to make it act like "wet" sand as evidenced by the vertical walls left in trenches dug by the surface sampler. Costes, et al. (1970) confirmed the bearing strength results by direct measurements on Apollo 11 lunar soil samples from Mare Tranquillitatis at the Lunar Receiving Laboratory.

It has been proposed that Van der Waals forces are responsible for the observed cohesion and that electrostatic charging could play some role. However, no satisfactory theory for the origin of a stable electrostatic component to lunar soil cohesion has been proposed. The purposes of this paper are to outline a theory in which electrostatic adhesion forces between lunar soil particles are produced and stabilized by solar ultraviolet irradiation, and to demonstrate that this could be the primary contributor to lunar soil cohesion.

If we assume that the moon is charged by solar radiation to a potential V (less than 10 volts positive) by photoelectric emission, the associated charge density is:

$$\frac{Q}{eA} = \frac{CV}{e4\pi R^2} = \frac{10/300}{4\pi(4.8 \times 10^{-10}) \times (1.74 \times 10^{8})} = 0.6 \text{ charges/cm}^2$$

where Q is the total charge, e is the charge of an electron, A is the surface area of the moon, C is the Moon's capacitance and R is the lunar radius.

With such a low average charge density, we can assume that macroscopically (20 μ scale), the charge density can fluctuate as long as the average macroscopic value is essentially zero.

Consider two particles lying side by side, Figure A-1, with work functions W_1 and W_2, respectively. At equilibrium the photoelectron currents ejected toward infinity $I_{1\infty}$ and $I_{2\infty}$ are balanced by returning electron fluxes $I_{\infty 1}$ and $I_{\infty 2}$. Similarly, the photoelectron currents between the two particles, I_{21} and I_{12}, cancel each other. This condition is satisfied only if surface charges exist on the two particles to compensate for the difference in work functions W_1 and W_2.

If a given locale is randomly disturbed (by meteorite impact for example) the currents ($I_{1\infty}$ and $I_{\infty 1}$, etc) from adjacent particles produced by solar UV radiation will be temporarily unequal since the electron Fermi level will vary with position due either to random orientation of particles, impact electrostatic charging, or secondary surface effects produced by recondensation of impact vaporized material.

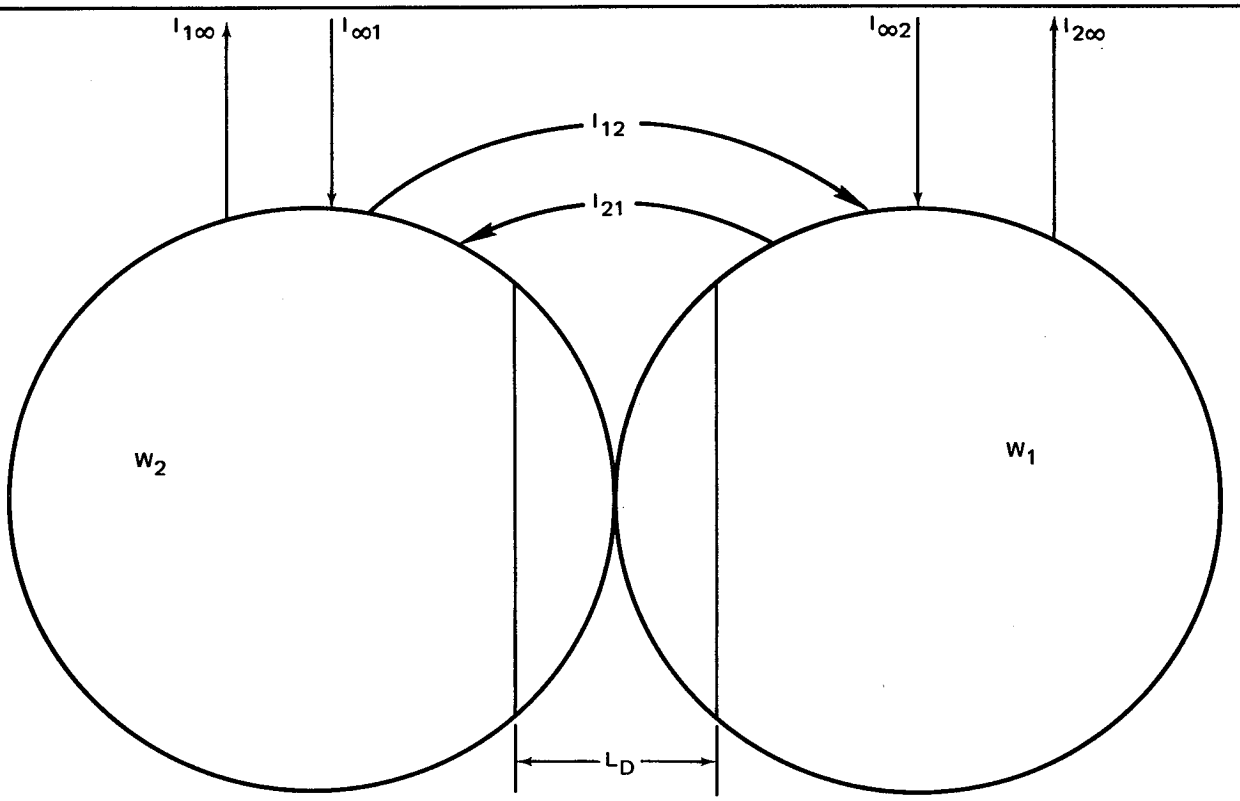

Figure A-1 Photoelectric Currents Produced on the Lunar Surface by Solar UV Radiation from Adjacent Particles with Different Work Functions W_1 and W_2

Charge will redistribute until the local area is again essentially electrically neutral and adjacent particle surface charges compensate for differences in work function. Charges can also transfer between particles by conduction at contracting asperites. Whatever the charge redistribution mechanisms are, the steady state space charge will be localized within the Debye length L_D from the surface or interface

$$L_D = \sqrt{\frac{\epsilon kT}{4\pi e^2 n}}$$

which depends only on n, the carrier charge density, and T, the absolute temperature. Here, k is Boltzman's Constant, and ϵ is the dielectric constant of the medium.

The electron charge density n can be estimated as follows. The electron generation rate, G, electrons cm^{-3} sec^{-1}, due to solar UV absorption between 100 nm and 300 nm is the product of the photon flux, 3×10^{15} photons cm^{-2} sec^{-1} (solar wind charging is much smaller and thus neglected), and the absorption coefficient, which beyond the absorption edge is typically $\alpha = 10^{+5}$ cm^{-1}. Thus, $G = 3 \times 10^{20}$ electrons cm^{-3} sec^{-1}. When a steady state is reached, the carrier generation rate, N_- electrons cm^{-3}, equals the recombination rate

$$G = RN_- = (\sigma V N_+)N_-$$

where $\sigma(cm^2)$ is the ionized site (N_+ sites cm^{-3}) electron capture cross section and V is the thermal electron velocity. Since $\sigma \cong 9 \times 10^{-16}$ and $V \cong 10^7$ cm/sec

$$(N_+ N_-)^{1/2} = N_- = \sqrt{G/\sigma V} \cong \sqrt{3 \times 10^{20}/10^{-15} \times 10^7}$$

$$N_- \cong 1.7 \times 10^{14}/cm^3$$

Solar cosmic ray damage could increase N_+ and decrease N_- by an order of magnitude or so. Therefore a value of $N_- = 1.7 \times 10^{13}$ charges cm^{-3} is probably a conservative value (Spenke, 1958). Setting $kT/e = 25.9$ mV, the Debye length is found to be

$$L_D = \sqrt{\frac{2.59 \times 10^{-3}}{300 \times 4\pi \times 4.8 \times 10 \times 1.5 \times 10^{14}}} = 500 \text{ Å}$$

This represents the thickness of the charge layer across which, at equilibrium, the electric field due to the space charge separation produces a voltage change equal to the work function difference between adjacent particles.

The adhesion force F due to electrostatic charges can be estimated by using the parallel plate capacitor formula

$$F = \frac{E^2}{4\pi E} = \frac{(W_2 - W_1)^2}{4\pi E L_D^2}$$

where E is the electric field. If two perfect dielectric spheres 20 microns in diameter touch at one point with a 0.1 volt difference in work function, the force of attraction for $L_D = 500$ Å would be 50 mdynes or approximately 15 times the Van der Waal's force.

As an example of the reality of this possibility Kottler et al. (1968) based on theoretical work by Krupp and Sperling (1966), demonstrated that triboelectrically charged 20 μ particles, with 2×10^{11} charges cm^{-2} adhere to an ultra-centrifuge rotor with forces over ten times greater than Van der Waals forces. Typically, the Van der Waal's component for this size particle, having asperites with 0.1 μm radii of curvature, is 3 mdyn.

When solar UV irradiation is stopped (during the lunar night for example) the space charge (which had been limited to within 500 Å of the particle surface) starts spreading deeper into the crystals, since L_D increases as the carrier density n decreases. During the 28-day lunar day, adhesion must

fluctuate with solar exposure about some mean value. However, lunar soil brought back by Apollo missions is permanently shielded from the charge stabilizing solar UV and X-ray irradiation. This increases the Debye length to a maximum value which can be estimated by assuming the resistivity is $\rho = 10^{12}\ \Omega\,cm$, and the mobility is 1 $cm^2\ volt^{-1}\ sec^{-1}$ which gives $n \simeq 10^7$ Therefore, L_D is on the order of 100 μm.

Since electrostatic adhesion is expected to decrease with time due to an increase in the photon shielded Debye length from 150 Å to 100 μm, the observed decrease in lunar soil adhesion with time at the Lunar Receiving Laboratory (Costes et al., 1970) can be partly accounted for.

The time constant τ can be estimated from the relation

$$\tau = \frac{\epsilon \rho}{4\pi}$$

which varies from 10 msec in the surface layer during solar irradiation and 100 days for $\rho = 10^{18}\ \Omega\,cm$. This latter figure is comparable to measured lifetimes of ultrahigh vacuum cleaved dielectrics (Ryan and Baker, 1967; Ryan et al. 1968; Grossman, 1969).

In the preceeding discussion we have not considered contamination and its interaction with the solar cosmic ray-damaged particle surfaces. These modify the electron affinity between particles which ultimately determines the force of adhesion; that is surface electrical double-layers change the apparent work functions of the two particles.

REFERENCES

Choate, R., S. A. Batterson, E. M. Christensen (Chairman), R. E. Hutton, L. D. Jaffe, R. H. Jones, H. Y. Ko, R. F. Scott, R. L. Spencer, F. B. Sperling, and G. H. Sutton (1968). Lunar Surface Mechanical Properties. Surveyor Program Results. NASA SP-184, National Aeronautics and Space Administration, Washington, D.C., 129-169.

Costes, N. V., W. D. Carrier, J. K. Mitchell, and R. F. Scott (1969). Apollo 11 Soil Mechanics Investigation. NASA SP-214 Apollo 11 Preliminary Science Report, National Aeronautics and Space Administration, Washington, D.C., 85-122.

Costes, N. C., W. D. Carrier, and R. F. Scott (1970). Apollo 11 Soil Mechanics Investigation. Science, Vol. 167, 739-741.

Grossman, J. J., Wegner, M. W. (1968). Exsolution Dislocations at Microperthite Boundaries in Orthoclase Trans. Amer. Geophys. Union, 49, 761.

Grossman, J. J. (1969). Electrostatic Charge Distribution on Ultrahigh Vacuum Cleaved Silicates, J. Vac. Sci. and Tech., 6, 233-236.

Grossman, J. J., Ryan, J. A., Mukherjee, N. R., Wegner, M. W. (1970). Microchemical Microphysical and Adhesive Properties of Lunar Material. Geochimica Et Cosmochimica Acta, Supplement I, Proceedings of the Apollo 11 Lunar Science Conference, Vol. 3, p. 2171-2181.

Kottler, W., H. Krupp, H. Rabenhorst (1968). Adhesion of Electrically Charged Particles. Z. Angew, Phys., 24, 219-223.

Krupp, H. and G. Sperling (1966). Theory of Adhesion, J. Appl. Phys. 37, 4176-4810.

McDonnell, J. D. C., Fleet, S. G. (1963). Direct Electron-Optical Resolution of Anti-phase Domains in a Silicate, Nature 199, 586.

Ryan, J. A. and M. B. Baker (1967). Adhesion Behavior of Air and Ultrahigh Vacuum Formed Silicate Surfaces in Relation to the Moon. Adhesion or Cold Welding of Materials in Space Environments. ASTM, STP 431, Phila., Pa., 234-237.

Ryan, J. A., J. J. Grossman, W. M. Hansen (1968). Adhesion of Silicates Cleaved in Ultrahigh Vacuum. J. Geophys. Res., 73, 6061-6070.

Scott, R. F. and F. I. Roberson (1969). Soil Mechanics Surface Sampler Surveyor Program Results, NASA SP-184, National Aeronautics and Space Administration, Washington, D.C., 171-179.

Spenke, E. (1958). Electronic Semiconductors (English Translation) McGraw Hill Book Co., New York, 334.

Wegner, M. W., Grossman, J. J. (1969). Dislocation Etching of Naturally Deformed Olivine, Trans. Amer. Geophys. Union 50, 676.